



Universiteit  
Leiden  
The Netherlands

## **A MeerKAT-meets-LOFAR study of Abell 1413: a moderately disturbed non-cool-core cluster hosting a 500 kpc 'mini'-halo**

Riseley, C.J.; Biava, N.; Lusetti, G.; Bonafede, A.; Bonnassieux, E.; Botteon, A.; ... ; Weeren, R.J. van

### **Citation**

Riseley, C. J., Biava, N., Lusetti, G., Bonafede, A., Bonnassieux, E., Botteon, A., ... Weeren, R. J. van. (2023). A MeerKAT-meets-LOFAR study of Abell 1413: a moderately disturbed non-cool-core cluster hosting a 500 kpc 'mini'-halo. *Monthly Notices Of The Royal Astronomical Society*, 524(4), 6052-6070. doi:10.1093/mnras/stad2218
















Version: Publisher's Version

License: [Creative Commons CC BY 4.0 license](https://creativecommons.org/licenses/by/4.0/)

Downloaded from: <https://hdl.handle.net/1887/3719126>

**Note:** To cite this publication please use the final published version (if applicable).

# A MeerKAT-meets-LOFAR study of Abell 1413: a moderately disturbed non-cool-core cluster hosting a $\sim 500$ kpc ‘mini’-halo

C. J. Riseley <sup>1,2,3\*</sup>, N. Biava <sup>1,2</sup>, G. Lusetti <sup>4</sup>, A. Bonafede <sup>1,2</sup>, E. Bonnasieux <sup>2,5,6</sup>, A. Botteon <sup>2</sup>, F. Loi <sup>7</sup>, G. Brunetti <sup>2</sup>, R. Cassano <sup>2</sup>, E. Osinga <sup>8</sup>, K. Rajpurohit <sup>1,2,9</sup>, H. J. A. Röttgering <sup>8</sup>, T. Shimwell <sup>8</sup>, R. Timmerman <sup>8</sup> and R. J. van Weeren <sup>8</sup>

<sup>1</sup>Dipartimento di Fisica e Astronomia, Università degli Studi di Bologna, via P. Gobetti 93/2, I-40129 Bologna, Italy

<sup>2</sup>INAF – Istituto di Radioastronomia, via P. Gobetti 101, I-40129 Bologna, Italy

<sup>3</sup>CSIRO Space and Astronomy, PO Box 1130, Bentley, WA 6102, Australia

<sup>4</sup>Hamburger Sternwarte, Universität Hamburg, Gojenbergsweg 112, D-21029 Hamburg, Germany

<sup>5</sup>Julius-Maximilians-Universität Würzburg, Fakultät für Physik und Astronomie, Institut für Theoretische Physik und Astrophysik, Lehrstuhl für Astronomie, Emil-Fischer-Str. 31, D-97074 Würzburg, Germany

<sup>6</sup>Observatoire de Paris, 5 place Jules Janssen, F-92195 Meudon, France

<sup>7</sup>INAF – Osservatorio Astronomico di Cagliari, Via della Scienza 5, I-09047 Selargius, CA, Italy

<sup>8</sup>Leiden Observatory, Leiden University, PO Box 9513, NL-2300 RA Leiden, the Netherlands

<sup>9</sup>Harvard-Smithsonian Center for Astrophysics, 60 Garden Street, Cambridge, MA 02138, USA

Accepted 2023 July 20. Received 2023 July 13; in original form 2023 May 31

## ABSTRACT

Many relaxed cool-core clusters host diffuse radio emission on scales of hundreds of kiloparsecs: mini-haloes. However, the mechanism responsible for generating them, as well as their connection with central active galactic nuclei, is elusive and many questions related to their physical properties and origins remain unanswered. This paper presents new radio observations of the galaxy cluster Abell 1413 performed with MeerKAT (L-band; 872 to 1712 MHz) and LOFAR HBA (120 to 168 MHz) as part of a statistical and homogeneous census of mini-haloes. Abell 1413 is unique among mini-halo clusters as it is a moderately disturbed non-cool-core cluster. Our study reveals an asymmetric mini-halo up to 584 kpc in size at 1283 MHz, twice as large as first reported at similar frequencies. The spectral index is flatter than previously reported, with an integrated value of  $\alpha = -1.01 \pm 0.06$ , shows significant spatial variation, and a tentative radial steepening. We studied the point-to-point X-ray/radio surface brightness correlation to investigate the thermal/non-thermal connection: our results show a strong connection between these components, with a superlinear slope of  $b = 1.63^{+0.10}_{-0.10}$  at 1283 MHz and  $b = 1.20^{+0.13}_{-0.11}$  at 145 MHz. We also explore the X-ray surface brightness/radio spectral index correlation, finding a slope of  $b = 0.59^{+0.11}_{-0.11}$ . Both investigations support the evidence of spectral steepening. Finally, in the context of understanding the particle acceleration mechanism, we present a simple theoretical model which demonstrates that hybrid scenarios – secondary electrons (re-)accelerated by turbulence – reproduce a superlinear correlation slope.

**Key words:** galaxies: clusters: general – galaxies: clusters: individual: Abell 1413 – galaxies: clusters: intracluster medium – radio continuum: general – X-rays: galaxies: clusters.

## 1 INTRODUCTION

Diffuse radio sources in clusters of galaxies trace the presence of non-thermal components – magnetic fields and relativistic electrons (or cosmic ray electrons, hereafter CRE) – on some of the largest scales in the Universe. Broadly speaking, these sources can be categorized into three principal classes dating back around two decades (e.g. Kempner et al. 2004): radio relics (also known as radio shocks or ‘radio gischt’), radio haloes, and radio mini-haloes (hereafter referred to simply as mini-haloes). As of 2019, a few hundred galaxy clusters had been detected which host some combination of radio relic(s)

and/or a radio halo (for the most recent observational review of these sources, see van Weeren et al. 2019).

With the advent of next-generation instrumentation such as the LOw-Frequency ARray (LOFAR; van Haarlem et al. 2013), the Murchison Widefield Array (MWA; Tingay et al. 2013), and the MeerKAT telescope (Jonas & MeerKAT Team 2016, though see also Camilo et al. 2018 and Mauch et al. 2020 for discussion of MeerKAT’s technical capabilities), the number of diffuse radio sources associated with clusters of galaxies is increasing rapidly (e.g. Botteon et al. 2018b, 2019, 2022; Wilber et al. 2018, 2020; Duchesne et al. 2020, 2021a, 2022; Locatelli et al. 2020; Biava et al. 2021; Duchesne, Johnston-Hollitt & Wilber 2021b; Duchesne, Johnston-Hollitt & Bartalucci 2021c; Hoang et al. 2021, 2022; Hoefl et al. 2021; Knowles et al. 2022; Riseley et al. 2022b; Venturi et al. 2022).

\* E-mail: [christopher.riseley@unibo.it](mailto:christopher.riseley@unibo.it)

Mini-haloes are perhaps the most elusive of the three canonical classes of diffuse radio source, with only some 35 currently catalogued, compared to some hundreds of relics and haloes. They are moderately extended radio sources, typically around 0.1–0.3 Mpc in size and are predominantly hosted by relaxed clusters. While relatively few mini-haloes have been catalogued to-date, statistical studies suggest that their occurrence rates are high among cool-core clusters, up to  $\sim 80$  per cent for massive clusters with  $M_{500} \gtrsim 6 \times 10^{14} M_{\odot}$ , although there is tentative evidence for a decreased rate among lower mass cool-core clusters (see discussion by Giacintucci et al. 2017).

The known population of mini-halo clusters is distributed across a broad range of redshifts from  $z \sim 0.01$  to  $z \sim 0.81$  (see van Weeren et al. 2019, and references therein). Due to the inefficient nature of the acceleration mechanism(s) responsible, relics, haloes, and mini-haloes all possess a steep radio spectrum, nominally  $\alpha \lesssim -1$  (where  $\alpha$  is the spectral index, relating flux density  $S$  to observing frequency  $\nu$  as  $S \propto \nu^{\alpha}$ ).

In the literature, there has been much discussion around the particle acceleration mechanism(s) that power mini-haloes. Broadly speaking, these fall into two classes: primary models (also known as the ‘turbulent (re-)acceleration’ scenario; Gitti, Brunetti & Setti 2002; ZuHone et al. 2013) and secondary models (also known as the ‘hadronic scenario’; Pfrommer & Enßlin 2004). For a review of all scenarios, see also Brunetti & Jones (2014).

Under the primary/turbulence scenario, electrons are accelerated to the relativistic regime (GeV energies) by cluster-scale magnetohydrodynamic (MHD) turbulence that is generated by core sloshing. In relaxed clusters, such core sloshing could be induced by dynamical interactions and/or minor/off-axis mergers with other clusters/groups. One of the most striking pieces of observational evidence for core sloshing comes from the detection of cold fronts and/or large-scale spiral motions in X-ray observations (Mazzotta et al. 2001a,b; Markevitch & Vikhlinin 2007; Mazzotta & Giacintucci 2008; Owers et al. 2009; Ghizzardi, Rossetti & Molendi 2010; Johnson et al. 2012; Paterno-Mahler et al. 2013; Rossetti et al. 2013; Ghizzardi, De Grandi & Molendi 2014; Botteon, Gastaldello & Brunetti 2018a; Savini et al. 2018; Riseley et al. 2022a). Such sloshing motions have also been investigated from the theoretical perspective (e.g. Ascasibar & Markevitch 2006; ZuHone et al. 2013).

In general, simulations have shown that these events can replicate several of the observed properties of clusters hosting mini-haloes, including large-scale bulk motions required to generate sloshing spirals (ZuHone et al. 2013; Machado & Lima Neto 2015) and fluctuations in radio spectral index that might be expected to arise from inhomogeneities in turbulence (Giacintucci et al. 2014). In recent years, much work has been devoted to exploring potential sources for the seed electrons. The co-location of many mini-haloes with a central radio brightest cluster galaxy (BCG) suggests a natural source for this population, and emerging correlations between the radio power of BCGs and mini-haloes, as well as mini-halo power and X-ray cavity power, provide observational support (Bravi, Gitti & Brunetti 2016; Richard-Laferrrière et al. 2020). While the BCG is commonly held to be the dominant factor in energy input into the ICM, recent work by Seth et al. (2022) has suggested that non-central radio galaxies may also provide a significant source of energy input into the ICM.

According to the secondary/hadronic scenario, CRe are continuously injected into the ICM through collisions between cosmic ray protons (CRp) and thermal protons. One of the natural sources of CRp in clusters are active galactic nuclei (AGNs); due to their longer

radiative lifetime, CRp are expected to persist throughout much of the cluster volume (Brunetti & Jones 2014).

Both scenarios share a number of commonalities, including (i) the important role of AGN, in particular the central BCG, and (ii) the connection between non-thermal and thermal components in the ICM. As such, investigating correlations between a number of observables – such as radio/X-ray surface brightness – is a key tool with which we can probe the underlying acceleration mechanism (e.g. Govoni et al. 2001).

With the established suite of Square Kilometre Array (SKA) Pathfinder and Precursor instruments, a number of recent works have begun to explore these correlations in increasing detail (Ignesti et al. 2020; Biava et al. 2021; Timmerman et al. 2021; Ignesti et al. 2022; Riseley et al. 2022a,b). In particular, Ignesti et al. (2020) studied point-to-point correlations for a first statistical sample of seven mini-haloes. The point-to-point correlation between radio surface brightness and X-ray surface brightness takes the form  $\log(I_R) \propto b \log(I_X)$ .

Giant radio haloes are generally believed to be generated by cluster-scale turbulence, and show a sub-linear correlation slope (i.e.  $b < 1$ ), which arises because both particles (acceleration and transport) and fields (amplification by turbulent-dynamo) follow the spatial distribution of turbulence, which is very broad. For point-to-point studies of radio haloes, see for example: Govoni et al. (2001), Brown & Rudnick (2011), Vacca et al. (2011), Rajpurohit et al. (2018, 2021a,b), Hoang et al. (2019), Botteon et al. (2020, 2023), Xie et al. (2020), Bruno et al. (2021), Hoang et al. (2021), Duchesne et al. (2021b), Bonafede et al. (2022), Vacca et al. (2022), Riseley et al. (2022b).

However, Ignesti et al. (2020) found a typically superlinear correlation slope (i.e.  $b > 1$ ) for their mini-halo sample. While a superlinear correlation slope arises naturally under the secondary/hadronic scenario, the primary/turbulence scenario can also replicate a superlinear correlation slope if either the CRe profile and/or the turbulence strength is more peaked toward the cluster centre. This would, however, suggest that mini-haloes trace a turbulent component that is different from the one powering giant haloes. As such, neither scenario is completely ruled out through point-to-point correlations alone.

Complicating our phenomenology, a growing number of mini-halo clusters show diffuse radio emission far outside the cool core, and far beyond any cold fronts/sloshing spiral structures (Venturi et al. 2017; Savini et al. 2018, 2019; Biava et al. 2021; Riseley et al. 2022a; Biava et al., in preparation). This challenges our theoretical understanding of particle acceleration mechanisms, which are typically confined to the sloshing regions (ZuHone et al. 2013, 2015).

One possibility is that hadronic interactions play an important role within the cool core, while turbulence becomes progressively dominant on larger scales (e.g. Cassano et al. 2012; Zandanel, Pfrommer & Prada 2014). The steep spectrum observed for diffuse emission outside the cool core in a handful of cases favours a turbulent acceleration interpretation (Savini et al. 2019; Biava et al. 2021).

### 1.1 The MeerKAT-meets-LOFAR mini-halo census

We are carrying out a census of all known radio mini-haloes in the Declination range  $-1^{\circ}$  to  $+30^{\circ}$  to determine the nature of particle acceleration mechanisms at play in mini-haloes using the first uniformly constructed mini-halo sample. The non-thermal window into our sample is provided by deep MeerKAT observations covering the frequency range 872–1712 MHz, and LOFAR HBA observations covering the frequency range 120–168 MHz. MeerKAT observations are being carried out under MeerKAT Project

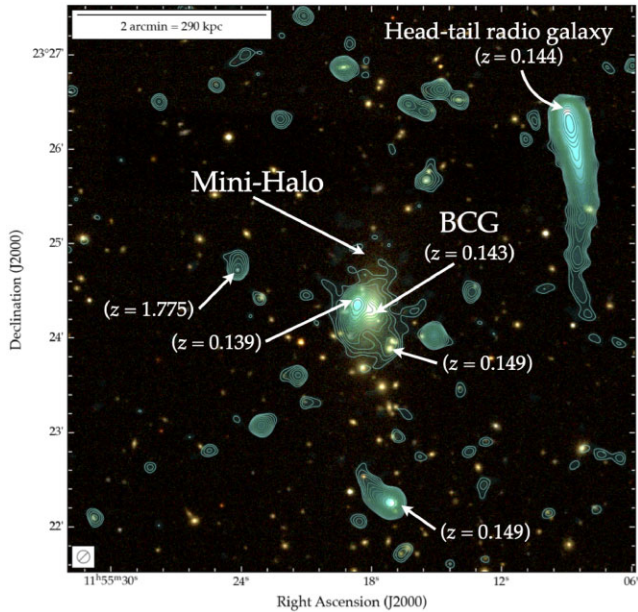


**Figure 1.** Colour-composite image of Abell 1413. The teal colourmap and contours represent the 1283 MHz radio surface brightness measured by MeerKAT at 8 arcsec resolution (teal colour and contours). Contours start at  $4\sigma$  and scale by a factor  $\sqrt{2}$ , where  $\sigma = 6.6 \mu\text{Jy beam}^{-1}$ ; see Table 1. The radio surface brightness is overlaid on an optical RGB image constructed using  $i$ -,  $r$ -, and  $g$ -band images from SDSS DR16 (Ahumada et al. 2020). The redshifts of selected galaxies are also shown for reference.

ID (PID) SCI-20210212-CR-01 (P.I. Riseley). LOFAR observations are sourced primarily from the LOFAR Two-metre Sky Survey (LoTSS; Shimwell et al. 2017, 2019, 2022) and expanded with targeted observations where LoTSS coverage is not yet completed. This multifrequency radio data set is augmented by archival X-ray data from *Chandra* and *XMM-Newton* to provide insights into the thermal properties of the mini-halo sample.

The first paper from this census detailed observations of the galaxy cluster MS 1455.0+2232 (Riseley et al. 2022a). To summarize the findings, we reported (i) the detection of significant diffuse radio emission on linear scales up to 586 kpc, far larger than previously reported, (ii) the detection of a sloshing spiral 254 kpc in extent, seen in the *Chandra* X-ray surface brightness gradient map, and (iii) a consistent superlinear slope in the point-to-point radio/X-ray surface brightness correlation. While both the primary/turbulence and secondary/hadronic scenarios were able to explain some of the observational properties of MS 1455.0+2232, neither could provide a fully satisfactory explanation of all the observed properties.

## 1.2 The galaxy cluster Abell 1413

In this paper, we report on another galaxy cluster selected for study as part of our census: Abell 1413. Fig. 1 shows a colour-composite image of this cluster, with the 1283 MHz radio surface brightness measured by MeerKAT overlaid on an optical RGB image constructed using  $i$ -,  $r$ -, and  $g$ -band images from Data Release 16 of the Sloan Digital Sky Survey (SDSS DR16; Ahumada et al. 2020).

Abell 1413 is an intriguing galaxy cluster at redshift  $z = 0.143$ , with a mass of  $M_{500} = (5.98^{+0.48}_{-0.40}) \times 10^{14} M_{\odot}$  (Planck Collaboration XVI 2014). This cluster has been the target of varied cosmological and galaxy evolution studies using multiwavelength data (e.g. Grainge et al. 2002; Morrison et al. 2003). At (sub-)mm

wavelengths, observations of the Sunyaev-Zeldovich (SZ) effect toward Abell 1413 suggest that the cluster exhibits an overall relaxed morphology (Grainge et al. 1996; Bonamente et al. 2006; LaRoque et al. 2006; AMI Consortium 2012), although there is a noticeable offset between the peak of the SZ signal and the peak of the X-ray emission corresponding to the thermal ICM (see discussion in AMI Consortium 2012).

Castagné et al. (2012) present a detailed optical analysis of the cluster-member galaxy population using data from SDSS DR7 (Adelman-McCarthy 2009) and new observations from the Canada–France–Hawaii Telescope. While the overall galaxy velocity distribution suggests a relaxed morphology, their analysis revealed several substructures within Abell 1413 that are broadly aligned along a North–South axis (see Castagné et al. 2012 for details).

At X-ray wavelengths, Abell 1413 has been studied extensively with various X-ray missions, including *XMM-Newton* and *Chandra* (Pratt & Arnaud 2002; Pointecouteau, Arnaud & Pratt 2005; Vikhlinin et al. 2005; Baldi et al. 2007; Snowden et al. 2008; Etori et al. 2010; Hoshino et al. 2010; Bartalucci et al. 2017; Botteon et al. 2018a; Lusetti 2021; Lusetti et al. 2023). Overall, Abell 1413 presents a slightly disturbed X-ray morphology, elongated in the North–South direction, although there is no strong evidence of a recent merger. The cluster has a higher central temperature ( $T_{\text{X}} = 8.3 \pm 0.2$  keV) and higher central entropy ( $K_0 = 64 \pm 8$  keV cm<sup>2</sup>) than expected for typical relaxed clusters (Giacintucci et al. 2017; Botteon et al. 2018a).

However, Abell 1413 shows a low centroid shift  $w = 0.04^{+0.01}_{-0.02}$  and a moderate concentration parameter,  $c = 0.44 \pm 0.04$  (both Campitiello et al. 2022) that are more typical of relaxed. We note that the definition of  $c$  used by Campitiello et al. (2022) differs from that adopted by e.g. Rossetti et al. (2017), who find  $c = 0.102 \pm 0.001$ . However, given the respective definitions of these metrics (see the discussions by those authors) the interpretation is the same: Abell 1413 overall shows a mixed X-ray morphology, neither fully relaxed nor disturbed.

Despite the lack of an identified cool core, Abell 1413 hosts a known mini-halo first identified as a candidate by Govoni et al. (2009) and later confirmed by Savini et al. (2019) using data from LOFAR High Band Antennas (HBA) at 145 MHz. The lack of a cool core is highly unusual for mini-halos: in the sample of Giacintucci et al. (2017), Abell 1413 is the only non-cool-core cluster to host a mini-halo. However, mini-halos hosted by non-cool-core clusters may be more common than this. Recent work from the MeerKAT Galaxy Cluster Legacy Survey (MGCLS; Knowles et al. 2022) reported the detection of seven clusters hosting newly detected candidate mini-halos and three confirmed new mini-halos, including Abell 4038 and MCXC J0342.8–5338 (Abell 3158). X-ray observations of these clusters reveal that neither shows typical characteristics of relaxed cool-core clusters. See respectively Rossetti & Molendi (2010) and Whelan et al. (2022) and references therein for discussion.

The ‘mini’-halo has also recently been studied using more recent LOFAR observations (Lusetti 2021; Lusetti et al. 2023) who found that the diffuse emission covers a larger physical scale at 145 MHz than previously thought, potentially up to  $\sim 800$  kpc in extent, and exhibits evidence of multiple components. These authors adopt the interpretation that Abell 1413 hosts a ‘mini-halo-plus-giant-halo’ type structure, although in this paper we will continue to refer to the entire diffuse source as a ‘mini’-halo.

The radio counterpart to the BCG of Abell 1413 was only recently reported for the first time by Savini et al. (2019). Previous higher frequency observations at 1.4 GHz achieved insufficient sensitivity to detect this faint source (Govoni et al. 2001; Giacintucci et al. 2017). Richard-Laferrrière et al. (2020) include Abell 1413 in their

sample of mini-haloes from which they re-derive scaling relations between mini-halo radio power and BCG radio power; however, with the available high-frequency radio data, they were only able to place limits on the radio power of the BCG at GHz frequencies. Finally, Abell 1413 was also recently studied as part of a mini-sample by Trehaeven et al. (2023) using relatively shallow MeerKAT observations. They report detections of both the radio counterpart to the BCG as well as the embedded head-tail radio galaxy at 1.28 GHz, as well as a measuring a linear size up to 211 kpc for the mini-halo. They also study the in-band spectral properties for these three sources, finding an ultra-steep in-band spectral index of  $\alpha = -1.52 \pm 0.46$ , although the uncertainty is large.

In this paper, we present new deep observations across the radio spectrum from 145 MHz to 1.7 GHz, taken with MeerKAT, the upgraded Giant Metrewave Radio Telescope (uGMRT; Gupta et al. 2017) and LOFAR HBA. The remainder of this paper is divided as follows: we discuss the observations and data reduction in Section 2, we present our results in Section 3 and analyse them in Section 4. We draw our conclusions in Section 6. Throughout, we assume a  $\Lambda$ CDM cosmology of  $H_0 = 73 \text{ km s}^{-1} \text{ Mpc}^{-1}$ ,  $\Omega_m = 0.27$ ,  $\Omega_\Lambda = 0.73$ . At the representative redshift of Abell 1413 ( $z = 0.143$ ; Sanders, Fabian & Smith 2011) the angular scale to linear size conversion is 1 arcsec to 2.417 kpc, with our cosmology. We quote all uncertainties at the  $1\sigma$  level.

## 2 OBSERVATIONS AND DATA REDUCTION

### 2.1 Radio: MeerKAT

Abell 1413 was observed with the MeerKAT telescope on two separate occasions: 2019 June 6 (CBID<sup>1</sup> 1565438457) and 2021 March 24 (CBID 1631864177). The 2019 observation was carried out under the ‘Mining Minihaloes with MeerKAT’ project (see Trehaeven et al. 2023), whereas the 2021 observation was carried out under our project, SCI-20210212-CR-01. Both observing runs were performed using the *L*-band receiver system, with 4096 channels covering the frequency range 872–1712 MHz.

The bandpass calibrator PKS B0407–658 was observed for 10 min at the beginning of each observing run; to track the time-varying instrumental gains, the compact radio source J1120+1420 was observed for 2 min at a quarter-hour cadence (CBID 1565438457) or half-hour cadence (CBID 1631864177). While the data from CBID 1565438457 have very recently been published by Trehaeven et al. (2023), our processing occurred independently, including our more recent observations which provided an overall increase in on-source time from 113 min (CBID 1565438457) to 5.6 h.

All observations from PID SCI-20210212-CR-01 were carried out with the intent of being calibrated in full polarization; to that end, the known polarization calibrator 3C 286 was observed for two 5-min scans during CBID 1631864177, separated by a broad parallactic angle range. No polarization calibrators were observed during CBID 1565438457.

Calibration was performed following the same steps as Riseley et al. (2022a). To summarize, initial calibration and flagging was carried out using the Containerized Automated Radio Astronomy Calibration (CARACAL) pipeline<sup>2</sup> (Józsa et al. 2020, 2021). CARACAL uses the Stimela framework (Makhathini 2018) as a wrapper

for standard-practice calibration tasks in the Common Astronomy Software Application (CASA) package.

We employed various flagging steps in CARACAL, including (i) shadowed antennas, (ii) specific channel ranges corresponding to the MeerKAT bandpass edges and known radio frequency interference (RFI) bands, and (iii) automatic sum-threshold flagging with the `tfcrop` algorithm. After initial calibration, we re-flagged our data with `tfcrop` and re-derived calibration tables to refine our solutions, and subsequently applied these to our target.

We then executed an initial round of relatively shallow automated sum-threshold flagging using TRICOLOUR<sup>3</sup> (Hugo et al. 2022). An initial sky model was generated using DDFACET (Tasse et al. 2018) and subtracted from our data; we then re-ran TRICOLOUR on the residual data to excise lower level RFI. Finally, we averaged to a spectral resolution of 1.67 MHz, yielding 512 output channels, and proceeded to self-calibration.

Throughout the self-calibration process, we imaged with DDFACET using `robust = -0.5` weighting (Briggs 1995), and employed the subspace deconvolution (SSD; Tasse et al. 2018) algorithm to improve the modelling of the numerous resolved radio sources across the field of view.

Self-calibration was performed using KILLMS (Tasse 2014; Smirnov & Tasse 2015). We carried out three rounds of phase-only self-calibration and two rounds of amplitude-and-phase self-calibration, both in direction-independent (DI) mode. As in Riseley et al. (2022a), we used the quality-based weighting scheme introduced by Bonnassieux et al. (2018) to weight our calibration solutions, which expedited the convergence of our self-cal process. After five rounds of DI self-calibration, our processing had largely converged and we inspected our image products for residual direction-dependent (DD) errors.

To correct for these DD errors, which were more naturally visible in the wider field, we tessellated the sky into 16 regions and carried out two rounds of DD-calibration and imaging, applying amplitude and phase gains on the fly. Finally, we generated an extracted data set covering a small region around our target by subtracting our best sky model of all sources outside the region of interest. Given that MeerKAT has a large primary beam full-width at half-maximum (FWHM), around 67 arcmin at 1.28 GHz (Mauch et al. 2020), this extraction step allowed us to efficiently post-process our data with manageable overhead.

### 2.2 Radio: Giant Metrewave Radio Telescope

Abell 1413 was observed with the uGMRT on two occasions using the GMRT Wideband Backend (GWB; Reddy et al. 2017) with the Band 3 receiver system, which covers the frequency range 250–500 MHz. Observations were carried out on 2020 October 3 (project 38.025; P.I. Cuciti) and 2022 April 22 (project 42.057; P.I. Biava) for a total on-source time of 7.8 h. We also observed Abell 1413 using the Band 4 receiver system in the frequency range 550–900 MHz on 2022 June 5 (project 42.057) for a total of 8 h on-source.

Using recent developments for wide-band data processing, these observations were processed using the Source Peeling and Atmospheric Modelling (SPAM; Intema et al. 2009, 2017) pipeline. To efficiently process the wide-band data and navigate limitations of the pipeline, the wide-band data are divided into smaller frequency sub-bands and calibrated independently. The pipeline initially derives calibration solutions from the primary calibrators and then applies

<sup>1</sup>Capture Block ID

<sup>2</sup><https://github.com/caracal-pipeline/caracal>

<sup>3</sup><https://github.com/ska-sa/tricolour>

them to the target field before proceeding to self-calibration. The self-calibration process corrects for both DI and DD calibration errors using a single reference model for all sub-bands, which is obtained by processing the narrow-band GMRT Software Backend (GSB) data recorded alongside the GWB data. The GSB data are processed using the standard SPAM pipeline. Finally, the calibrated GWB visibilities then ready for post-processing using other software tools, as described in Section 2.5.

We note that in this paper we only present high-resolution images from our uGMRT data. The presence of several bright resolved radio galaxies in the wider field limits the dynamic range and image fidelity of our data products, despite our use of the well-verified SPAM software to perform initial data processing and self-calibration. This effect is particularly pronounced on short baselines, and is worse in Band 4 due to the decreased primary beam FWHM. Techniques for post-processing SPAM-calibrated data sets are under development but their application is beyond the scope of this paper. We will revisit this data set in future as part of a wider follow-up campaign of mini-haloes, including the ‘MeerKAT-meets-LOFAR’ sample.

### 2.3 Radio: LOFAR HBA

Abell 1413 was observed with LOFAR as part of LoTSS, and performed using the full International LOFAR Telescope (ILT; van Haarlem et al. 2013) in HBA\_DUAL\_INNER mode, covering the frequency range 120–168 MHz. Three LoTSS fields overlap Abell 1413 (P177+22, P178+25, P180+22); however, due to particularly poor ionospheric conditions during observations of P178+25, only the data for P177+22 and P180+22 are used in this work. These two fields are separated from Abell 1413 by an angular distance of 1.68 and 1.95 deg, respectively. P177+22 was observed on 2017 May 4; P180+22 was observed on 2017 August 9. We note that these are different observations to those presented by Savini et al. (2019), although this is fundamentally the same set of observations presented by Lusetti (2021) and Lusetti et al. (2023); we have undertaken an independent post-processing.

In this work, we only make use of the LoTSS data from the Dutch LOFAR array (Core and Remote stations, encompassing baselines out to  $\sim 80$  km). The full ILT observations presented in Riseley et al. (2022a) of MS 1455.0+2232 showed that a significant amount of the flux from the radio counterpart to the BCG was lost due to the relatively faint nature of the source; in Abell 1413, the radio galaxies embedded in the mini-halo are significantly fainter than the radio BCG in MS 1455.0+2232, and thus we do not expect to make a high signal-to-noise ratio detection with the full ILT.

The Dutch LOFAR array data were processed using the standard LoTSS pipeline,<sup>4</sup> which is described in detail by Shimwell et al. (2019, 2022) and Tasse et al. (2021). As a brief summary, this pipeline performs flagging, initial calibration, and both DI and DD self-calibration using KILLMS and DDFACET. An extracted data set was then created, containing a region within 0.35 deg radius around Abell 1413 using the process described by van Weeren et al. (2021) to allow for efficient re-imaging with different weighting schemes and  $uv$ -selection ranges.

### 2.4 Ancillary radio data

To provide additional flux density measurements for radio sources of interest, we turned to ancillary data. This included a 3 GHz mosaic

image from the Karl G. Jansky Very Large Array (VLA) Sky Survey (VLASS; Lacy et al. 2020), sourced via the Canadian Initiative for Radio Astronomy Data Analysis (CIRADA) image cutout server. The radio counterpart to the BCG is undetected in the VLASS mosaic, although we note a marginal detection of a source that may be correspond to the radio core of the embedded head-tail radio galaxy.

In addition, we used the  $L$ -band (1008–1968 MHz) VLA images of Abell 1413 recently presented by Osinga et al. (2022). These observations were taken as part of project 15A–270, and were performed on 2015 February 2 with the VLA in B configuration, for a total on-source time of 40 min. We refer the reader to Osinga et al. (2022) for details of the data processing steps. Note that these observations were not used to study the diffuse emission of the mini-halo, due to the limited sensitivity to extended low surface-brightness emission of the VLA B-configuration observations; instead, these data were used to provide flux density measurements for the various radio galaxies in the vicinity of Abell 1413 – principally the BCG.

### 2.5 Radio post-processing

We followed the same post-processing steps as Riseley et al. (2022a). In brief, we used WSCLEAN (Offringa et al. 2014; Offringa & Smirnov 2017) version 2.10.0<sup>5</sup> to generate science-quality images from our extracted MeerKAT, LOFAR, and uGMRT data sets.

We used multiscale clean in order to optimally model the diffuse emission present in the field. We cleaned using the `-auto-mask` and `-auto-threshold` functionality to automate the deconvolution, and used the `-join-channels` and `-channels-out` options to improve the wide-band deconvolution, producing Stokes  $I$  sub-band images across the bandwidth, in addition to multifrequency-synthesis (MFS) images at frequencies of 1283 MHz for MeerKAT, 145 MHz for LOFAR, 400 MHz for uGMRT Band 3, and 675 MHz for uGMRT Band 4.

We also employed a common inner  $uv$ -cut of  $80\lambda$  for all data sets. This choice reduces contamination from Galactic emission and residual RFI by deselecting baselines between the two substations of each LOFAR HBA Core Station.

Finally, we performed three rounds of additional DI self-calibration on our MeerKAT data using the LOFAR Default Pre-Processing Pipeline (DPPP; van Diepen, Dijkema & Offringa 2018). In each round, we solved for a diagonal gain matrix. Further self-calibration did not yield appreciable improvement. LOFAR data undergo DI self-calibration as part of the extraction process; as such, further self-calibration did not yield appreciable improvement.

Final representative low- and high-resolution images were produced by varying the `robust` parameter between different WSCLEAN imaging runs. We used `robust = -0.5` for low-resolution imaging and `robust = -2.0` (corresponding to uniform weighting) for high-resolution imaging. For our uGMRT data, we use only high-resolution images made with `robust = -2.0` to study the spectral properties of the nearby compact sources, in particular the embedded radio BCG.

#### 2.5.1 Flux scaling

LOFAR observations and uGMRT observations that are processed using the SPAM pipeline are tied to the Scaife & Heald (2012) flux scale, which is consistent with the Kellermann (1966) scale above

<sup>4</sup>[github.com/mhardcastle/ddf-pipeline/](https://github.com/mhardcastle/ddf-pipeline/)

<sup>5</sup>WSClean is available at <https://gitlab.com/aroffringa/wsclean>

325 MHz. The MeerKAT data presented in this work had the flux density scale set using observations of PKS B0407–658, and so these data are tied to the Baars et al. (1977) scale. To convert our MeerKAT data to be consistent with the Scaife & Heald (2012) scale, we use a polynomial fit to the values presented in table 7 of Baars et al. (1977), performed in log-linear space. This polynomial fit yielded a conversion factor of 0.968 at the reference frequency of our MeerKAT observations ( $\nu_{\text{ref}} = 1283$  MHz).

We also used established routines to verify the flux scale of our extracted LOFAR images through comparison with the well-verified LoTSS flux scale. This routine is described in detail elsewhere (Hardcastle et al. 2016; Shimwell et al. 2019, 2022), but in brief, we generated an image at 6 arcsec resolution using WSCLEAN and extracted a catalogue using the Python Blob Detection and Source Finder software (PYBDSF; Mohan & Rafferty 2015), which was compared with a point-source-filtered catalogue derived from the full-field LoTSS image, before performing a linear regression best fit in the flux:flux plane. Overall, this routine yielded a bootstrapping factor of 1.156 to align with the LoTSS flux scale. Finally, we adopt a typical 5 per cent uncertainty in our MeerKAT flux scale; and a representative 10 per cent uncertainty in our LOFAR flux scale (following Shimwell et al. 2022). We also adopt a 10 per cent systematic uncertainty in our GMRT flux scale.

### 2.5.2 Source subtraction and final imaging

Several compact or partially resolved sources are visible in the region of the mini-halo in Abell 1413, including the compact radio source associated with the BCG (see Fig. 1) and the nearby head-tail radio galaxy embedded in the mini-halo. Subtraction of these contaminating sources was necessary to fully explore the diffuse emission of the mini-halo.

We followed the same process as Riseley et al. (2022a) and subtracted the clean component model corresponding to these sources. To generate this model, we imaged with WSCLEAN, applying an inner  $uv$ -cut of  $5k\lambda$  to filter the diffuse emission of the mini-halo. This scale corresponds to an angular scale of 41 arcsec or a linear scale of 99 kpc, and was chosen as it effectively suppressed our recovery of the mini-halo without reducing sensitivity to emission from the embedded head-tail radio galaxy (which has a projected largest angular size of 35 arcsec at 1283 MHz).

After subtracting these clean component model of these sources in the  $uv$ -plane, we generated source-subtracted images using WSCLEAN as per Section 2.5. We produced images at 15 arcsec resolution by using  $\text{robust} = -0.5$  in conjunction with appropriate  $uv$ -tapering and subsequent image-plane smoothing. Properties of all radio maps presented in this work are listed in Table 1.

## 2.6 X-ray: Chandra

To provide the critical window into the thermal properties of the ICM of Abell 1413, we used X-ray data from *Chandra* using the Advanced CCD Imaging Spectrometer I-array (ACIS-I) instrument. Abell 1413 has been observed with *Chandra* ACIS-I on five occasions (ObsIDs 537, 1661, 5002, 5003, 7696) for a total net exposure time of 128 ks, although some of these ObsIDs are off-axis. These data have been previously presented in Botteon et al. (2018a), and we refer the reader to this paper for full details of the data processing steps; we use the surface brightness and temperature maps originally presented by those authors in this work. Later in this paper we show these maps in Fig. 9 to aid context.

We note that Botteon et al. (2018a) performed an edge searching using a Gaussian Gradient Magnitude (GGM; Sanders et al. 2016) filter, which suggested some discontinuities but were not supported by surface brightness profile fits. As with Riseley et al. (2022a), we further explored the ICM surface brightness distribution by applying an adaptive GGM filter (Sanders et al. 2022) to the *Chandra* mosaic. Unlike our previous investigation of MS 1455.0+2232 (Riseley et al. 2022a) however, no statistically significant edges were found which could indicate the presence of a large-scale sloshing spiral. Therefore we do not present images of our adaptive-GGM filtered map in this paper.

## 3 RESULTS

### 3.1 Radio continuum properties

We present our final full-resolution (8 arcsec) maps of Abell 1413 in Fig. 2 at reference frequencies of 1283 MHz (MeerKAT; left-hand panel) and 145 MHz (LOFAR; right-hand panel). These maps respectively have an rms noise of 6.6 and  $164 \mu\text{Jy beam}^{-1}$ .

Through a combination of deeper observations and the application of our advanced data processing recipes, we achieve greater sensitivity compared to previously published studies. Our LOFAR maps at 145 MHz show a factor  $\sim 2$  improvement in rms at 145 MHz compared to Savini et al. (2019), who report  $270 \mu\text{Jy beam}^{-1}$  at  $\sim 10$  arcsec resolution. However, we note that this is a factor  $\sim 2$  worse than the median rms noise of  $83 \mu\text{Jy beam}^{-1}$  at 6 arcsec resolution achieved by LoTSS DR2 (Shimwell et al. 2022). This largely reflects the reduction in sensitivity of aperture arrays like LOFAR when observing at low elevation; such an increase in typical rms can also be seen in fig. 2 of Shimwell et al. (2022) for example. Our MeerKAT 1283 MHz map shows a  $\sim 70$  per cent improvement in rms compared to Trehaven et al. (2023), who report  $11.2 \mu\text{Jy beam}^{-1}$  at a resolution of  $(12.2 \times 5.9)$  (arcsec  $\times$  arcsec); alternatively, our MeerKAT map is around a factor 15 more sensitive than the results reported by Govoni et al. (2009) at a similar frequency.

The high sensitivity of our MeerKAT data enable us to detect many compact radio galaxies in the vicinity of Abell 1413. Beyond these sources, we also recover the moderately extended head-tail radio galaxy embedded in the mini-halo emission, a second tailed radio galaxy directly to the south of the cluster, as well as the known extended head-tail radio galaxy to the west of the cluster, first reported by Savini et al. (2019). These sources are clearly visible in Figs 1 and 2, for example.

Comparatively, our LOFAR map shows fewer sources in the vicinity. Of the compact sources detected by MeerKAT, only a handful are detected at above  $4\sigma$ . These sources are likely active radio galaxies with typical spectral index values flatter than our ‘noise spectral index’ (essentially the steepest spectral index a source detected at 1283 MHz would have while still remaining detectable at 145 MHz), which is around  $-1.5$ . Deeper observations with LOFAR would be required to measure their spectral properties.

Overall, the mini-halo is only moderately recovered at 8 arcsec resolution in each map. Some hints of the extended emission are visible in the coherent structure of the local noise, albeit below the  $4\sigma$  level, and are also visible in Fig. 1. However, given the extended structure of the embedded head-tail radio galaxy as well as the nearby compact radio sources, these contaminants must be excised before performing analysis of the diffuse mini-halo.

We also report the properties of these sources, including their reference coordinates, flux density measurements, and optical cross-identifications (where available) in Table A1. For compact sources,

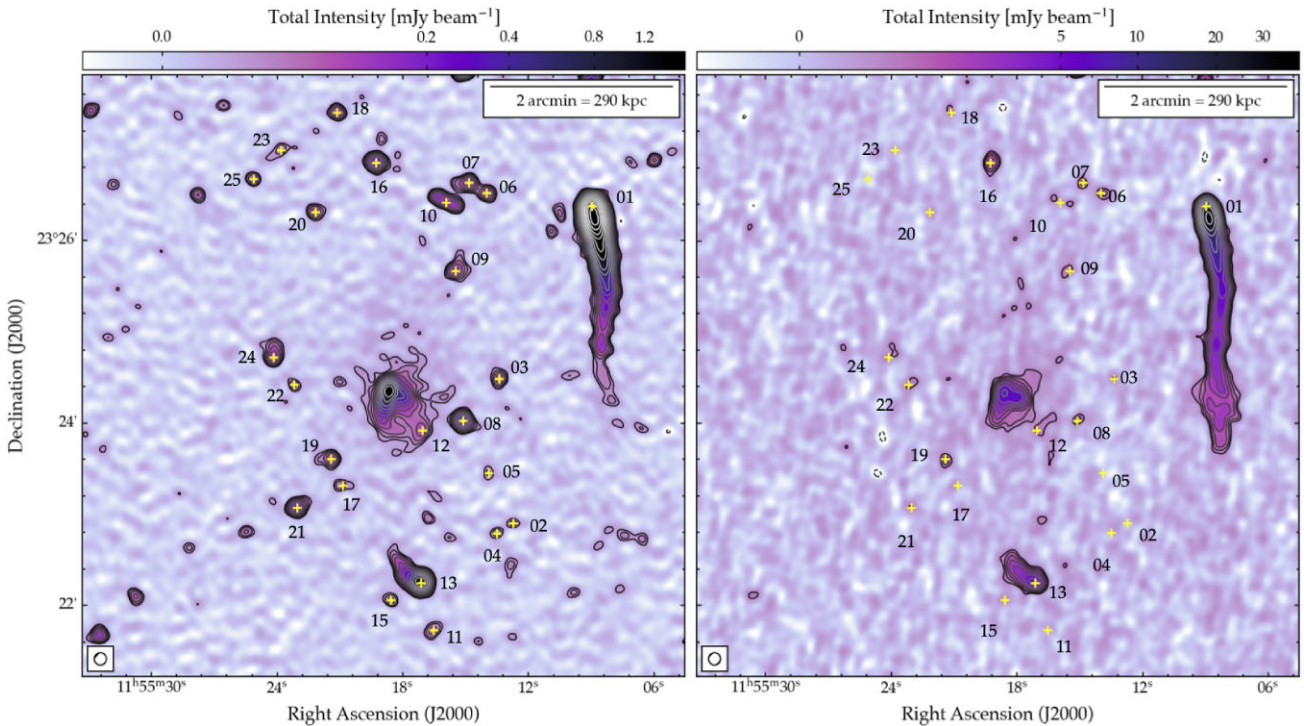


**Figure 2.** Radio continuum images of Abell 1413 with MeerKAT at 1283 MHz (left-hand panel,  $\text{robust} = -0.5$ ), LOFAR HBA at 145 MHz (right-hand panel,  $\text{robust} = -1.0$ ) at 8 arcsec resolution. Contours start at  $4\sigma$  and scale by a factor  $\sqrt{2}$ , where  $\sigma = 6.6 \mu\text{Jy beam}^{-1}$  at 1283 MHz, and  $164 \mu\text{Jy beam}^{-1}$  at 145 MHz. The dashed contour denotes the  $-3\sigma$  level. Yellow ‘+’ signs identify sources referred to in Table A1, along with their associated ID numbers, except the embedded head-tail radio galaxy (source 14). All identified sources were subtracted when generating our low-resolution images, with the exception of source 01.

the reference coordinates are given as the best-fitting position; for resolved sources, the reference coordinate is the best fit to the centroid of the brightest component (typically believed to be the radio core).

### 3.2 Source-subtracted images

Fig. 3 presents our images of Abell 1413 at 15 arcsec resolution, after subtracting the contaminating compact and marginally resolved radio galaxies identified in Fig. 2. These images were produced using a combination of  $uv$ -tapering and image-plane convolution to achieve this resolution. At 15 arcsec resolution, we measure an rms noise of  $6.9 \mu\text{Jy beam}^{-1}$  with MeerKAT at 1283 MHz and  $192 \mu\text{Jy beam}^{-1}$  with LOFAR at 145 MHz.

The enhanced sensitivity to diffuse emission provided by these techniques allows us to detect the extended mini-halo with high significance in Fig. 3. The mini-halo is extended and highly asymmetrical, being elongated along a North–South axis, similar to the disturbed BCG, and following the same axis as both the galaxy substructure (Castagné et al. 2012) and the X-ray surface brightness distribution. This has also been commented on by previous radio studies (Savini et al. 2019; Lusetti 2021; Trehaeven et al. 2023).

In both our MeerKAT and LOFAR source-subtracted maps, it is curious to note that the mini-halo appears to be divided into two slightly distinct regions. The inner region of the mini-halo, close to the BCG,<sup>6</sup> appears brighter and marginally more regular, whereas the larger scale diffuse emission extends further and is clearly fainter and more diffuse. This may hint at the presence of multiple components,

<sup>6</sup>Within a radius of 21 arcsec, or 50.7 kpc given our cosmology.

similar to a handful of other cases reported in recent years from studies of relaxed clusters using next-generation interferometers (e.g. Savini et al. 2018, 2019; Biava et al. 2021; Riseley et al. 2022a).

The total extent of contiguous emission above the  $3\sigma$  level in our MeerKAT map provides a largest angular size (LAS) of 242 arcsec, equivalent to a largest linear size (LLS) of 584 kpc at the cluster redshift, given our cosmology. This overlaps with a region of faint emission to the south where we cannot exclude the possibility of some residuals associated with the southern tailed radio galaxy; excluding this region we measure a LAS of 186 arcsec (LLS of 449 kpc). Our LLS measurements indicate that the mini-halo in Abell 1413 is at least twice as large as previously measured by Govoni et al. (2009), who reported a angular size of 90 arcsec (around 220 kpc).

Measuring similarly in our LOFAR map, we recover a LAS around 142 arcsec, equivalent to 343 kpc. Similarly to our previous work on MS 1455.0+2232, the apparent decrease in size at 145 MHz is likely related to the relative sensitivity of our MeerKAT and LOFAR maps. The relative sensitivity places a lower limit on the spectral index of  $-1.53$  in regions where MeerKAT measures emission from the mini-halo but LOFAR does not; this is not in tension with the expected spectral index of the mini-halo based on recent detailed studies with high-quality data (e.g. Biava et al. 2021; Riseley et al. 2022a).

We note that while the extent of the diffuse emission measured from our LOFAR maps is smaller than the  $\sim 800$  kpc extent reported by (Lusetti 2021; Lusetti et al. 2023) using fundamentally the same LOFAR observations, the results are not in tension. Those authors present a lower resolution study focused on mapping the extent of the ‘mini’-halo, hence adopting a lower threshold of  $2\sigma$  and more naturally weighted imaging parameters. Our study is focused on



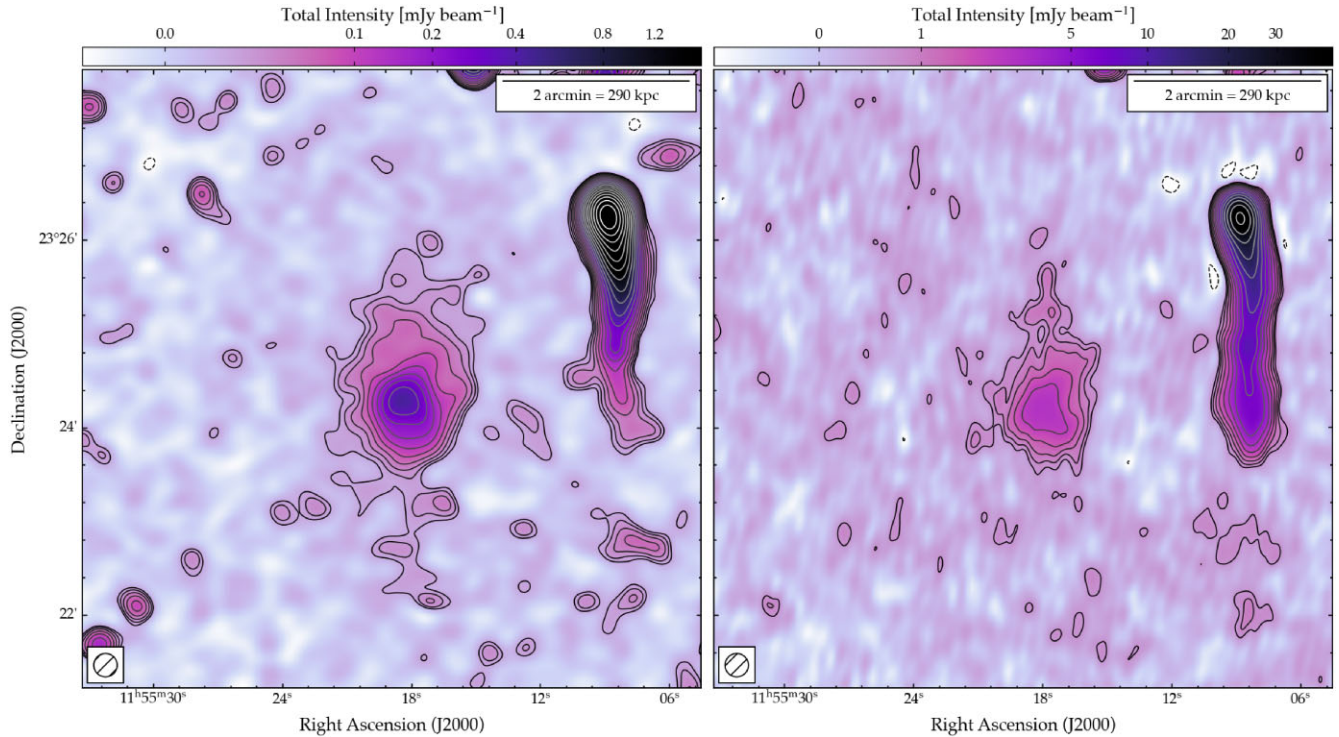


**Figure 3.** Source-subtracted radio continuum images of Abell 1413 with MeerKAT at 1283 MHz (left-hand panel) and LOFAR HBA at 145 MHz (right-hand panel) at 15 arcsec resolution. Contours start at  $3\sigma$  and scale by a factor  $\sqrt{2}$ , where the respective value of  $\sigma$  is listed in Table 1. The dashed contour denotes the  $-3\sigma$  level.

**Table 1.** Summary of image properties for images of Abell 1413. Images marked with a † were produced after source-subtraction, with the application of a  $uv$ -taper to achieve the desired resolution. The quoted RMS noise values were derived as the average of several off-source regions in the vicinity of the phase centre.

Telescope	Freq. (GHz)	Robust	RMS noise ( $\mu\text{Jy beam}^{-1}$ )	Resolution (arcsec)	PA ( $^\circ$ )
VLA	1.512	0.0	18.2	$4.0 \times 3.1$	34
MeerKAT	1.283	-0.5	6.6	8	0
		-2.0	23.7	$6.7 \times 2.9$	178
		-0.5†	6.9	15	0
uGMRT	0.675	-2.0	17.8	$3.5 \times 2.5$	64
	0.400	-2.0	47.1	$6.1 \times 3.0$	54
LOFAR	0.145	-0.5	163	8	0
		-2.0	566	$3.9 \times 2.6$	102
		-0.5†	192	15	0

understanding the nature of the particle acceleration mechanism via the spectral properties, and hence we adopt a higher threshold of  $3\sigma$  and more robust-weighted imaging parameters to allow for a more spatially-resolved spectral study. When common imaging settings are used, the results are consistent.

### 3.3 The brightest cluster galaxy in Abell 1413

Fig. 4 shows a zoom on the central region of Abell 1413, where the BCG and companion head-tail radio galaxy are visible. We overlay radio contours from our high-resolution maps. The BCG itself, catalogued in the literature as MCG+04-28-097 (Noonan 1972), is a large cD galaxy with extremely high ellipticity (Castagné

et al. 2012) at redshift  $z = 0.1429$  (Humason, Mayall & Sandage 1956).

The BCG is detected at high significance in our MeerKAT, JVLA, and uGMRT maps in addition to our LOFAR map, where the signal-to-noise ratio is lower due to the reduced sensitivity of LOFAR when adopting uniform weighting. The embedded head-tail radio galaxy is also detected at high significance in our JVLA, MeerKAT, and uGMRT maps; only the presumed core of this head-tail is detected by LOFAR in Fig. 4.

We used these to measure the flux density of the (unresolved) radio counterpart to the BCG. These measurements are listed in Table 2 and presented in Fig. 5; they indicate no departure from a single power-law behaviour between 145 MHz and 1.519 GHz. We fitted a single power-law model to the data, from which we derive a spectral index  $\alpha = -1.13_{-0.06}^{+0.07}$ .

This spectral index is steeper than that measured for ‘typical’ active radio galaxies outside of cluster environments, which generally show a canonical synchrotron spectral index of around  $-0.8$ . It is also significantly steeper than that measured for the BCG of MS 1455.0+2232, which was shown to exhibit a spectral break in our first MeerKAT-meets-LOFAR paper (Riseley et al. 2022a). There the spectral index below the break was very flat,  $\alpha_{\text{low}} = -0.45 \pm 0.05$ , and above the spectral break more typical of ‘standard’ field radio galaxies  $\alpha_{\text{low}} = -0.81 \pm 0.18$ .

However, some radio galaxies in cluster environments show evidence of similarly steep spectra (e.g. Riseley et al. 2022b) although this is more typical of emission in the extended lobes rather than the active cores. In their survey of the radio properties of BCGs, Hogan et al. (2015) find a representative spectral index of  $-1.0$  for the ‘non-core’ component of BCG radio emission, which comprises ‘all other emission’ besides the core, largely constituting lobe emission and past AGN activity. As such, given the steep spectrum of

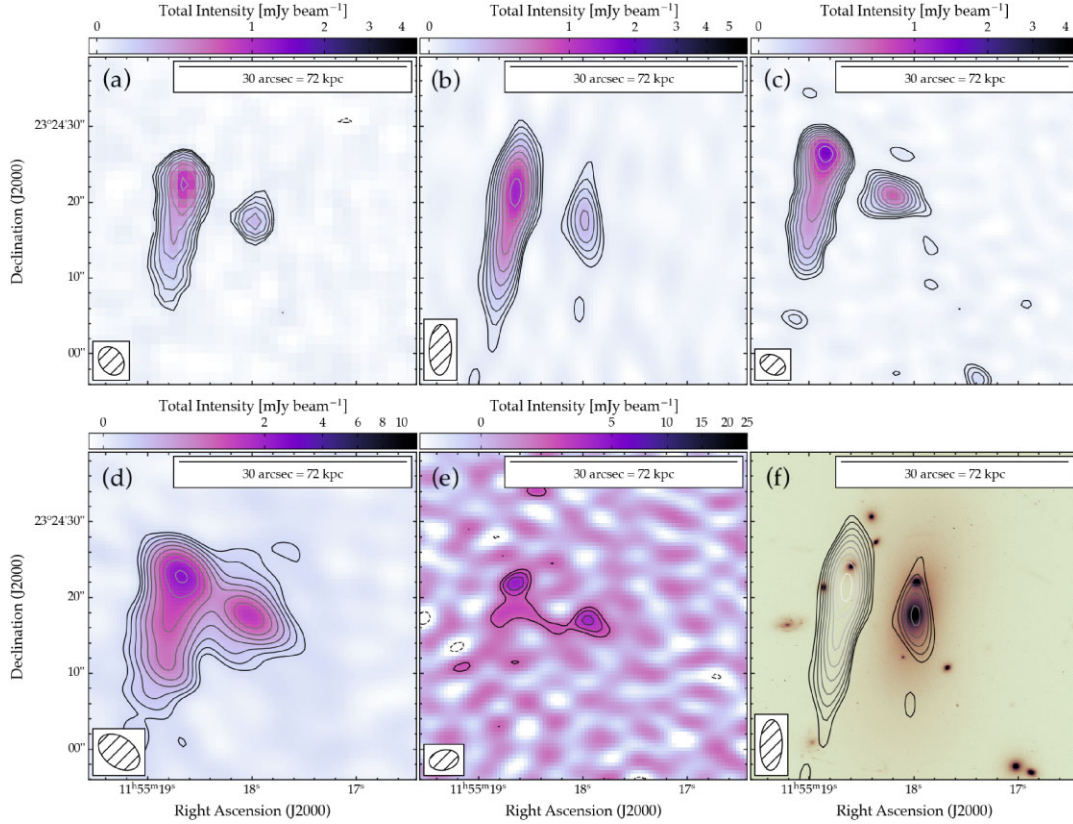


**Figure 4.** Zoom on the BCG of Abell 1413. Panels (a) through (e) show radio data as both colourmaps and contours, whereas panel (f) shows an *HST* WFPC2 image, combining data from the *F850LP* and *F775W* filters overlaid with MeerKAT radio data from panel (b). The radio data shown are as follows: VLA data at 1519 MHz (panel a), MeerKAT data at 1283 MHz (panel b), uGMRT Band 4 data at 675 MHz (panel c), uGMRT Band 3 data at 400 MHz (panel d) and LOFAR data at 145 MHz (panel e). All radio maps were produced using `robust` =  $-2.0$  weighting, except in panel (a), where `robust` =  $0$  weighting was used. All contours start at  $3\sigma$  increment by a factor of  $\sqrt{2}$ , where  $\sigma$  is listed in Table 1.

**Table 2.** Flux density measurements for the unresolved radio counterpart to the BCG in Abell 1413. All measurements quoted on the Scaife & Heald (2012) flux density scale.

Frequency (GHz)	Flux density (mJy)
1.519	$0.27 \pm 0.02$
1.283	$0.30 \pm 0.02$
0.675	$0.63 \pm 0.05$
0.400	$1.20 \pm 0.14$
0.145	$3.78 \pm 0.75$

$\alpha = -1.13^{+0.07}_{-0.06}$  we measure for the radio counterpart to the BCG in Abell 1413, we consider it more likely that this radio source is lobe-dominated in comparison to the radio counterpart to the BCG in MS 1455.0+2232, which is likely core-dominated.

The  $k$ -corrected radio power  $P_\nu$  at frequency  $\nu$  is expressed as:

$$P_\nu = 4\pi D_L^2 S_\nu (1+z)^{-(1+\alpha)}, \quad (1)$$

where  $D_L$  is the luminosity distance to the object and  $S_\nu$  is the flux density at frequency  $\nu$ . In the case of the BCG in Abell 1413, the redshift  $z = 0.1429$  implies  $D_L = 650.7$  Mpc given our cosmology. Thus, equation (1) yields a 1.4 GHz radio luminosity of  $P_{1.4 \text{ GHz}} = (1.46 \pm 0.07) \times 10^{22} \text{ W Hz}^{-1}$  for the radio counterpart to the BCG of Abell 1413.

## 4 ANALYSIS: THE MINI-HALO IN ABELL 1413

### 4.1 Spectral properties

#### 4.1.1 Integrated spectrum

Measuring the total integrated flux density for the mini-halo in Abell 1413 is non-trivial due to the likely imperfect subtraction of the head-tail radio galaxy to the south of the cluster. We defined the extent of the mini-halo to be bounded by the contiguous  $3\sigma$  contour, as measured by MeerKAT and presented in the left-hand panel of Fig. 3, but excluding the southern extremity.

Integrating over this region, MeerKAT recovers a total flux density of  $S_{1283 \text{ MHz}} = 3.23 \pm 0.17$  mJy. For LOFAR, we measure a total integrated flux density of  $S_{145 \text{ MHz}} = 29.5 \pm 3.4$  mJy. Thus, our integrated spectral index for the mini-halo in Abell 1413 is  $\alpha_{145 \text{ MHz}}^{1283 \text{ MHz}} = -1.01 \pm 0.06$ .

This is somewhat flatter than the estimated spectral index of  $\alpha_{144 \text{ MHz}}^{1400 \text{ MHz}} \sim -1.3$  reported by Savini et al. (2019). This discrepancy is unsurprising, as Savini et al. do not provide an uncertainty estimate, and additionally the 1.4 GHz measurement used by those authors was the VLA flux density measurement from Govoni et al. (2009), whereas our MeerKAT maps are demonstrably more sensitive. Trehaeven et al. (2023) report a MeerKAT in-band spectral index of  $\alpha_{1 \text{ GHz}}^{1.5 \text{ GHz}} = -1.52 \pm 0.46$  for the mini-halo in Abell 1413, which is broadly consistent with our integrated spectrum, although their uncertainty is large.

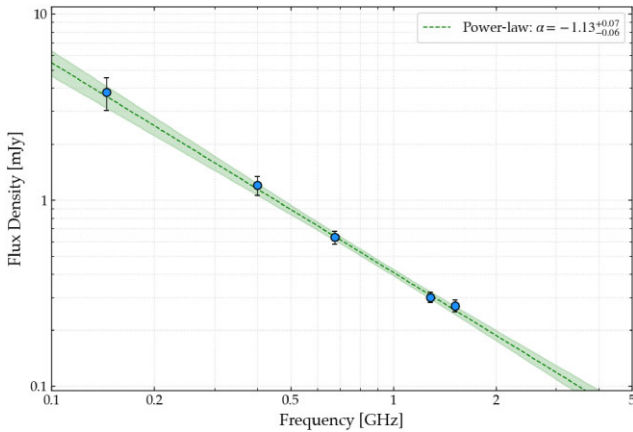


**Figure 5.** Integrated spectral energy distribution for the unresolved radio BCG in Abell 1413. The blue datapoints indicate new measurements made on our data. The dashed line and shaded region, respectively, represent the best-fitting power-law spectral index and the uncertainty region corresponding to the 16th and 84th percentiles:  $\alpha = -1.13^{+0.07}_{-0.06}$ .

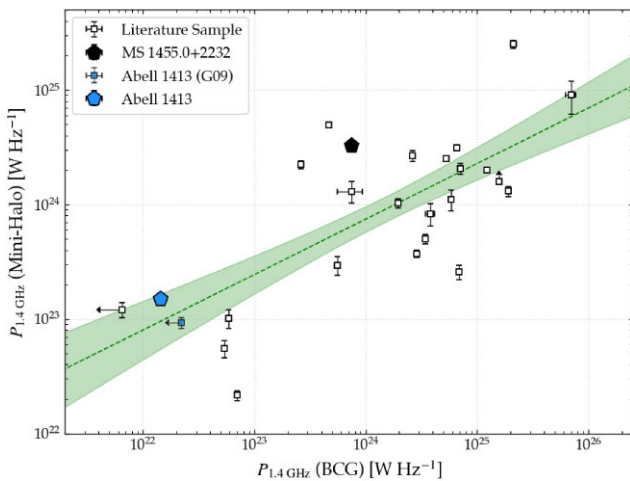


**Figure 6.** Scaling plane between BCG radio power and mini-halo radio power at 1.4 GHz. Our new measurements for Abell 1413 are shown by the blue pentagon; the blue square indicates the previous measurements and limits on the mini-halo and BCG radio power, respectively, from Govoni et al. (2009). The measurements for MS 1455.0+2232 are from Riseley et al. (2022a). The ‘Literature Sample’ comprises the sample of Giacintucci et al. (2019) plus the mini-halo candidate reported by Norris et al. (2021). Uncertainties in the radio power for Abell 1413 and MS 1455.0+2232 are not visible at this scale. The dashed line denotes the best-fitting scaling relation, which exhibits a slope of  $m = 0.48^{+0.11}_{-0.11}$ ; the shaded region indicates the  $1\sigma$  uncertainty on the slope.

Looking beyond this cluster at the broader population, this is consistent with the spectral index measured for MS 1455.0+2232 ( $-0.97 \pm 0.05$ ; Riseley et al. 2022a) and similar to several other clusters studied with the latest generation of radio interferometers (e.g. Raja et al. 2020; Biava et al. 2021; Timmerman et al. 2021), which enable studies to be performed with improved surface brightness sensitivity, resolution, and dynamic range.

#### 4.1.2 Luminosity and scaling relations

Using the integrated flux density measurements and spectral index derived in the previous section, and taking the luminosity distance at

the cluster redshift  $D_L = 651.2$  Mpc, equation (1) yields a 1.4 GHz radio power of  $P_{1.4 \text{ GHz}} = (1.50 \pm 0.08) \times 10^{23} \text{ W Hz}^{-1}$  for the mini-halo.

To compare our radio power measurement with the known population, we used the most recent compilation of mini-haloes from Giacintucci et al. (2019), updated with our measurement for MS 1455.0+2232 (Riseley et al. 2022a) and the mini-halo candidate reported in the Evolutionary Map of the Universe (EMU; Norris et al. 2011) Pilot Survey region (Norris et al. 2021). We show the known population in the power scaling plane between BCG radio power and mini-halo radio power at 1.4 GHz in Fig. 6. This power scaling plane allows us to explore the relation between mini-haloes and AGN feedback processes driven by the BCG. In a scenario where the BCG plays some role in powering mini-haloes, such as by driving turbulence through mechanical feedback and/or by seeding cosmic rays in the ICM, we would expect to observe a correlation. This was explored for the first time in detail by Richard-Laferrière et al. (2020), who found a moderate-strength correlation in this plane.

For context, we also show the position of the mini-halo in Abell 1413 using the measurements reported by Govoni et al. (2009). We note that these authors did not detect the radio counterpart to the BCG at 1.4 GHz but as such reported an upper limit to the BCG radio power.

We opted to use LINMIX<sup>7</sup> (Kelly 2007) to fit a scaling relation for the BCG and MH radio power, both at 1.4 GHz, as shown in Fig. 6. Scaling relations for similarly statistically significant MH populations have been derived in relatively recent years by Richard-Laferrière et al. (2020), although using differing methods: the perhaps more ‘classic’ BCES-orthogonal and BCES-bisector. However, those authors fit the relation using two different abscissas: the ‘BCG steep’ radio power at 1 GHz and the ‘BCG core’ radio power at 10 GHz. In our census we do not have the data to distinguish clearly between these components and instead derive our scaling relation using the total BCG radio power measured at 1.4 GHz from our broad-band data. We derived this using a power-law relation in log–log space of the form:

$$\log(P_{1.4 \text{ GHz}}(\text{MH})) = a + m \log(P_{1.4 \text{ GHz}}(\text{BCG})) \quad (2)$$

finding a best-fitting slope of  $m = 0.48^{+0.11}_{-0.11}$ . We find that these two quantities exhibit a moderate-to-strong correlation, as we find Spearman and Pearson coefficients of  $r_s = +0.56$  and  $r_p = +0.71$ , respectively. We find a stronger correlation than previously reported by Giacintucci et al. (2019), for example, who found  $r_s = +0.43$ . This increase in correlation strength is likely dominated by the improved sample size considered, as our results show consistency with the correlation strength reported by Richard-Laferrière et al. (2020):  $r_s = +0.53$  and  $r_p = +0.68$  for the scaling between MH power at 1.4 GHz and BCG-steep radio power at 1 GHz.

From Fig. 6 we can see that our new measurements place Abell 1413 toward the faint end of the power scaling plane. The position is not dramatically shifted with respect to previous measurements from Govoni et al. (2009), and thus Abell 1413 remains among the faintest mini-haloes in the known population.

#### 4.1.3 Resolved spectral properties

In Fig. 7 we report the spatially resolved spectral index map between 1283 and 145 MHz at 15 arcsec resolution, along with the associated uncertainty. While detailed investigation of the entire mini-halo

<sup>7</sup>Currently available at <https://linmix.readthedocs.io/en/latest/src/linmix.html>.

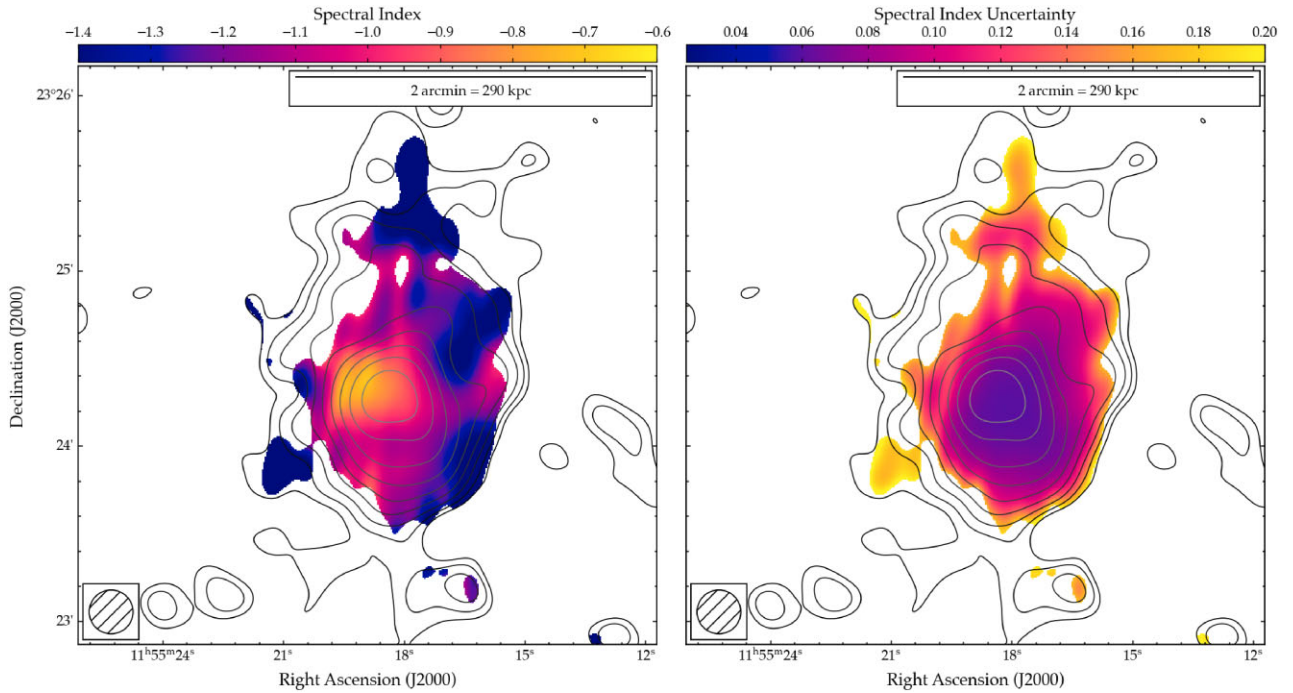


**Figure 7.** Spectral index (left-hand panel) and associated uncertainty (right-hand panel) of Abell 1413 between 145 and 1283 MHz at 15 arcsec resolution, made from our source-subtracted maps presented in Fig. 3. Contours denote the source-subtracted MeerKAT data at 1283 MHz, starting at  $3\sigma$  and scaling by a factor  $\sqrt{2}$ .

volume is somewhat limited by the reduced sensitivity of our LOFAR data relative to our MeerKAT data, we can still study the resolved spectral properties of much of the mini-halo.

From Fig. 7, when measuring across the entire mini-halo we find an overall median spectral index of  $\langle\alpha\rangle = -1.18 \pm 0.11$ , consistent with our integrated spectral index derived in Section 4.1.1. However, this does not tell the whole story, as the spectral index map appears to show two distinct trends.

The inner region of the mini-halo close to the BCG (within 21 arcsec, or 50.7 kpc) which appears brighter and more uniform in surface brightness, seems to show a distinct trend separate from the more extended diffuse emission. This inner region appears to show a generally flatter spectral index around  $-0.7$  to  $-1$  whereas the larger scale diffuse emission appears to show a typical spectral index around  $-1.1$  or steeper.

Measuring the median spectral index both inside and outside this ‘brighter region’ we find  $\langle\alpha_{\text{in}}\rangle = -0.97 \pm 0.07$  and  $\langle\alpha_{\text{out}}\rangle = -1.12 \pm 0.13$ . While these values are barely consistent at the  $\sim 1\sigma$  level, it suggests tentative evidence of radial steepening in the spectrum of the MH. Additionally, the significance is likely greater, as this uncertainty estimate includes the systematic uncertainty; accounting only for the *statistical* uncertainty (as flux scale errors would not affect the *relative* spectral index) would likely increase the significance.

The lower limit to the spectral index in these outer regions derived based on the relative sensitivity of our MeerKAT and LOFAR data does not provide powerful constraints in the outermost regions, as these regions must have  $\alpha \gtrsim -1.53$  given that they are detected by MeerKAT but not LOFAR. Deeper low-frequency observations would be required to examine this further as we are currently limited by the quality of the available LOFAR HBA data. However, this does suggest that there is no ultrastep spectrum highly diffuse component as observed in some other cases (e.g. Biava et al. 2021).

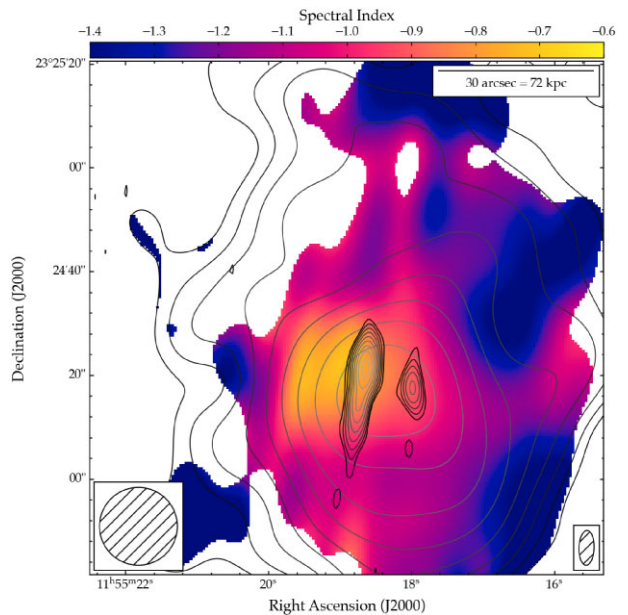


**Figure 8.** Zoom on the spectral index map of Fig. 7, showing the central region around the embedded radio galaxies. Contours show the low-resolution source-subtracted MeerKAT surface brightness at 15 arcsec resolution as well as the high-resolution MeerKAT surface brightness from our *robust -2* weighted maps, showing the embedded radio sources. The beam sizes of each map are indicated in the lower left-hand and lower right-hand corners, respectively.

Fig. 8 presents a zoom on the spectral index map in the left-hand panel of Fig. 7, with our high-resolution MeerKAT map (Fig. 4, panel b) overlaid as contours. From this figure, we see that the region of flatter spectrum within the MH is offset to the East of the embedded

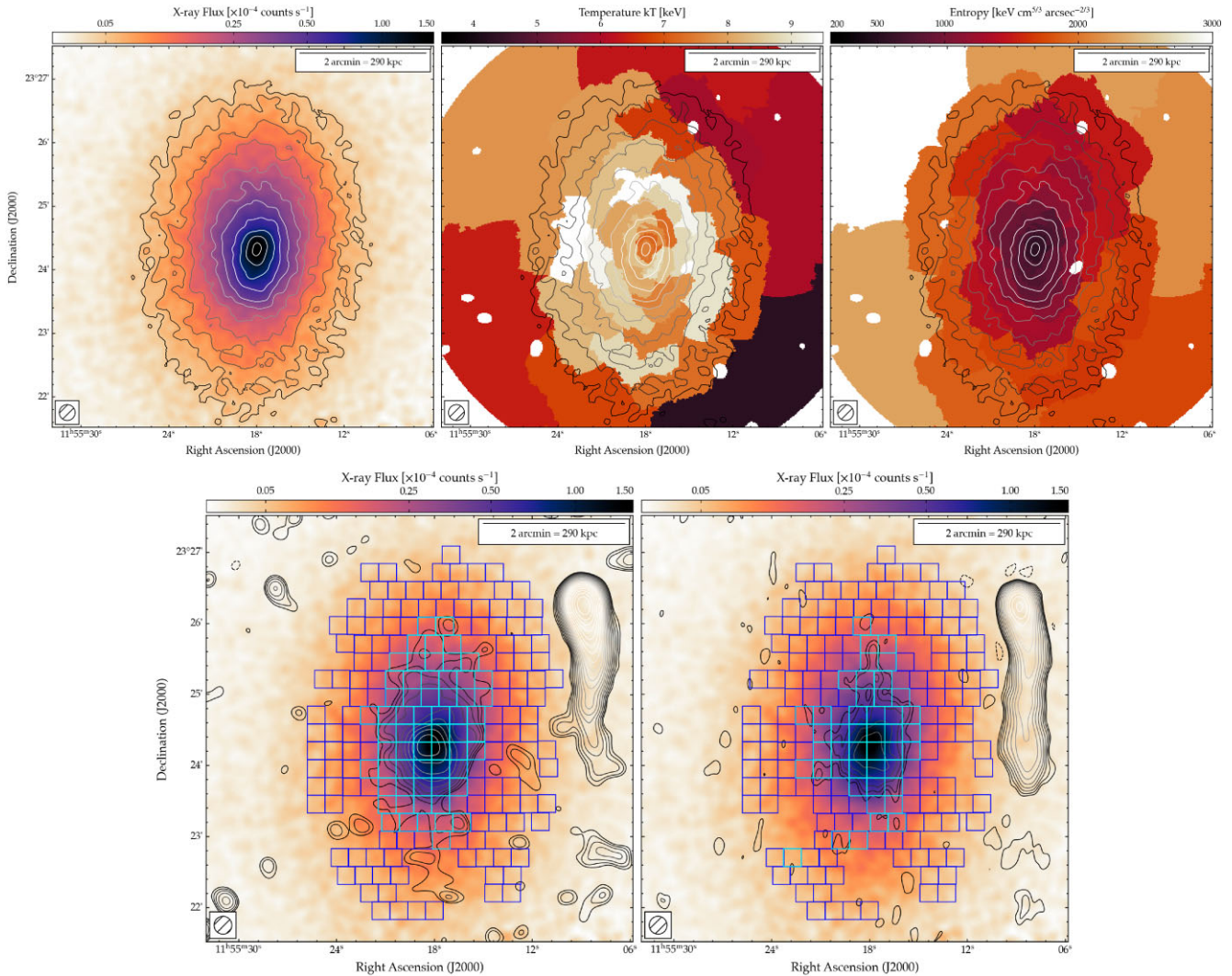


**Figure 9.** Radio/X-ray overlay images of Abell 1413. Top row: X-ray surface brightness in the 0.5–2 keV band measured by *Chandra*, smoothed with a 15 arcsec FWHM Gaussian (left-hand panel); ICM pseudo-temperature (centre); pseudo-entropy (right-hand panel). These maps were derived and presented in fig. 15 of Botteon et al. (2018a) and are shown here to aid context. Contours show the X-ray surface brightness starting at  $5 \times 10^{-6}$  counts  $s^{-1}$  and scaling by a factor of  $\sqrt{2}$ . With a central temperature of  $kT \simeq 7.5$  keV and central entropy of  $K \simeq 564$   $keV cm^{5/3} arcsec^{-2/3}$ , Abell 1413 exhibits characteristics that are neither typical of fully relaxed or merging clusters. Bottom row: The colour map shows the X-ray surface brightness as per the left-hand panel in the upper row. Contours denote source-subtracted radio data at 15 arcsec resolution as per Fig. 3 (left: MeerKAT at 1283 MHz; right: LOFAR at 145 MHz). The boxes show the 15 arcsec square regions used to profile the radio/X-ray correlations: the cyan and blue boxes show regions where the radio surface brightness is above and below  $3\sigma$  level, respectively.

radio sources, in particular the head-tail radio galaxy. As such, we consider it unlikely that this region indicates the presence of residual emission from an inadequate source model, but rather represents a flatter spectrum component of diffuse emission within the MH.

#### 4.2 Thermal/non-thermal comparison

Observationally, both radio haloes and mini-haloes follow a similar morphology to the X-ray ICM. Given this connection, we expect a correlation between the observational properties of the *non-thermal* components – the CRE and magnetic field, traced by the diffuse synchrotron emission – and the *thermal* components – the hot plasma of the ICM, traced by the bremsstrahlung X-ray emission.

Fig. 9 presents a radio/X-ray overlay of Abell 1413. In the top row we show the X-ray surface brightness measured by *Chandra* as well as the X-ray pseudo-temperature (kT) and pseudo-entropy (K) maps

originally presented by Botteon et al. (2018a) to provide context for the reader. In the bottom row we show the X-ray surface brightness with our source-subtracted radio contours overlaid. As expected, the mini-halo fills much of the volume of the X-ray emitting ICM. To quantitatively explore the thermal/non-thermal connection, we placed adjacent 15 arcsec square boxes across the extent of the X-ray emission recovered by *Chandra*, above a level of  $5 \times 10^{-6}$  counts  $s^{-1}$ . However, to avoid contamination from imperfect subtraction of the more complex sources in the vicinity of the mini-halo, we excised those regions where residuals above the  $3\sigma$  level remained. Our final region set is also shown in Fig. 9. Following previous works, we adopted a  $2\sigma$  level as the threshold between measurements and limits; regions where the average radio surface brightness was above the  $2\sigma$  level we took as measurements (cyan boxes in Fig. 9), regions where the average radio surface brightness was below this level we took as  $2\sigma$  limits (blue boxes in Fig. 9). In each case, we use the

median value of the appropriate quantities in each region to examine the correlations; in each case, changes in the placement of the regions have no significant effect on the fit result.

#### 4.2.1 Point-to-point correlation: surface brightness

Fig. 10 presents the radio/X-ray surface brightness correlation – the  $I_R/I_X$  plane – for Abell 1413, as measured from the regions shown in Fig. 9. Our data appear to show a strong and positive correlation between  $I_R$  and  $I_X$ , reflecting the nature of the correlation between the non-thermal and thermal components.

Indeed, we find Spearman and Pearson coefficients of  $r_S = +0.90$  and  $r_P = +0.94$  at 1283 MHz and  $r_S = +0.84$  and  $r_P = +0.86$  at 145 MHz, indicating a very strong correlation. To quantify the slope of the correlation, we fit a power-law relation (in log–log space) of the form:

$$\log(I_R) = c + b \log(I_X), \quad (3)$$

where the slope  $b$  quantifies the scaling between the thermal and non-thermal components of the ICM. This slope is related to the underlying particle acceleration mechanism responsible for the diffuse synchrotron emission (Govoni et al. 2001; Brunetti et al. 2004; ZuHone et al. 2013, 2015).

In general, a superlinear slope is expected in the secondary/hadronic scenario, due to the central CRp injection profile and relative scaling between the CR and thermal gas (see e.g. Ignesti et al. 2020). In the primary/turbulent (re-)acceleration scenario, depending on the nature and distribution of CRe throughout the cluster volume, either a sublinear or superlinear slope can be generated.

We used LINMIX (Kelly 2007) to determine the best-fitting values of  $b$  and  $c$ . LINMIX takes a hierarchical Bayesian approach to linear regression, accounting for uncertainties on both the independent and dependent variables – in this case,  $I_X$  and  $I_R$  respectively – as well as upper limits. This latter aspect is important, as the diffuse radio emission recovered by MeerKAT and LOFAR does not fill the entirety of the X-ray emitting volume of Abell 1413.

LINMIX yields a best-fitting slope of  $b_{1283 \text{ MHz}} = 1.63^{+0.10}_{-0.10}$  and  $b_{145 \text{ MHz}} = 1.20^{+0.13}_{-0.11}$ . Note that we take the median value from our linear regression as the best-fitting value, and use the 16th and 84th percentiles to define the uncertainty. Thus, there is clear evidence of a change in slope with frequency, at  $\gtrsim 3.4\sigma$  significance. There is no evidence of departure from a single correlation in the  $I_R/I_X$  plane which might signify differences in the physical conditions and/or emission mechanism (as in Biava et al. 2021; Riseley et al. 2022a). The results of our fitting routine are also summarised in Table 3.

As a further investigation, to account for the relative sensitivity of each of our data sets, we re-ran our LINMIX fitting routine in the  $I_R/I_X$  plane using a common set of regions where the radio surface brightness was measured to be in excess of  $2\sigma$  at both 1283 and 145 MHz. Regions where the radio surface brightness  $I_R$  was less than  $2\sigma$  at either frequency were treated as upper limits in the same manner, adopting a value of  $2\sigma$  in the respective map. We found a superlinear correlation with steeper slope of  $b_{1283 \text{ MHz}} = 2.23^{+0.22}_{-0.19}$  and  $b_{145 \text{ MHz}} = 1.36^{+0.15}_{-0.11}$ , confirming the change in correlation slope.

#### 4.2.2 Point-to-point correlation: spectral index

We also studied the spatial distribution of the radio spectral index, and the connection with the thermal properties of Abell 1413, via point-to-point analysis of the correlation between spectral index  $\alpha$  and X-ray surface brightness, i.e. the  $\alpha/I_X$  plane.

Fig. 11 presents the  $\alpha/I_X$  correlation plane for Abell 1413, profiled using the same regions shown in Fig. 9. Limits are more difficult to account for when considering the  $\alpha/I_X$  plane, as both upper and lower limits to the spectral index can be present depending on the relative sensitivity of the radio data and the underlying physical processes. See also discussion by Botteon et al. (2020).

As is visible in Fig. 7, there are a number of regions toward the mini-halo outskirts where we cannot measure the spectral index, due to the limited sensitivity of the LOFAR data. While we could place a lower limit on the spectral index for these regions, these are non-trivial to account for even with a Bayesian algorithm such as LINMIX. Thus, we performed our point-to-point analysis using only regions where spectral index measurements were possible: those regions above the  $3\sigma$  level in both radio maps.

Fig. 11 appears to show a good correlation between  $\alpha$  and  $I_X$ ; indeed, we find that the measurements are strongly correlated with correlation coefficients  $r_S = 0.67$  and  $r_P = 0.62$ . Again, we used LINMIX to perform the linear regression, fitting a power law in log-linear space as follows:

$$\alpha = c + b_\alpha \log(I_X). \quad (4)$$

Our linear regression yields a best-fitting slope of  $b_\alpha = 0.59^{+0.11}_{-0.11}$ ; this slope is plotted in Fig. 11, with the  $1\sigma$  uncertainty traced by the shaded region. We observe no sign of departure from a single trend in the  $\alpha/I_X$  plane, in line with the observed spectral steepening in the spatially resolved spectral index map presented in Fig. 7.

#### 4.2.3 Point-to-point correlation: discussion

Few mini-haloes in the literature have the necessary highly sensitive multifrequency radio data with which to examine both the  $I_R/I_X$  and  $\alpha/I_X$  planes. Two examples are the mini-haloes hosted by RX J1720.1+2638 and MS 1455.0+2232 (respectively Biava et al. 2021; Riseley et al. 2022a). Among a sample of seven mini-haloes, Ignesti et al. (2020) reports dual-frequency investigation of the  $I_R/I_X$  for two clusters, Abell 3444 and 2A 0335+096, using historic narrow-band data; however, those authors do not study the  $\alpha/I_X$  correlation.

Biava et al. (2021) analyse the point-to-point correlations for the multiple diffuse components hosted by RX J1720.1+2638: the known mini-halo and eastern extension, as well as the larger scale diffuse emission seen only at LOFAR frequencies. These three components show clearly distinct trends, with the mini-halo showing a superlinear slope in the  $I_R/I_X$  plane, and the others showing a sublinear slope. In the  $\alpha/I_X$  plane, the mini-halo shows no correlation, whereas the other components each follow a single distinct correlation. For MS 1455.0+2232, the  $I_R/I_X$  plane is characterized by a single correlation, whereas regions inside and outside the sloshing spiral showed different behaviour in the  $\alpha/I_X$  plane (see Riseley et al. 2022a).

Aspects of our findings for Abell 1413 are similar. The correlation in the  $\alpha/I_X$  plane for Abell 1413 is similar to the behaviour outside the sloshing spiral in MS 1455.0+2232, where the correlation slope was  $b_\alpha = 0.21 \pm 0.11$ . Similarly, the single correlation in the  $I_R/I_X$  plane is consistent with our findings for MS 1455.0+2232.

While the observed superlinear slope in the  $I_R/I_X$  plane is typical of mini-haloes, it is not yet conclusive whether the frequency dependence of this slope is the norm. In this case of Abell 1413, the correlation slope clearly changes with frequency. The mini-halo in 2A 0335+096 shows tentative evidence of a slope change with frequency, although the presence of substructures within the mini-halo means that the uncertainties are large (see Ignesti et al. 2020, 2022). Abell 3444, RX J1720.1+2638, and MS 1455.0+2232 show

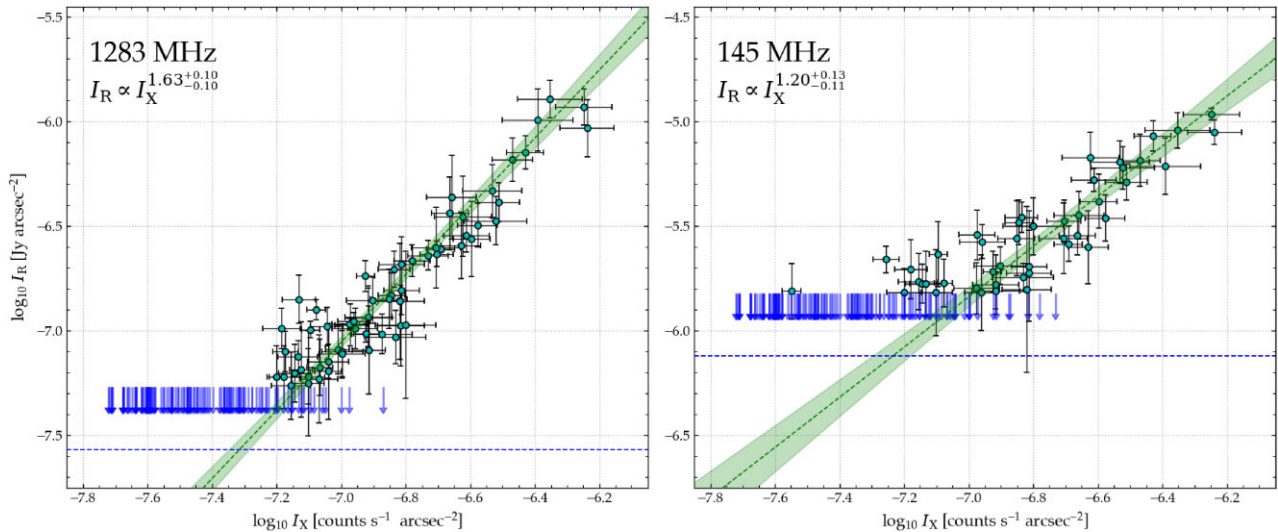


**Figure 10.** Radio/X-ray surface brightness correlation ( $I_R/I_X$ ) for the mini-halo in Abell 1413 at 1283 MHz (left-hand panel) and 145 MHz (right-hand panel) at 15 arcsec resolution. Datapoint markers are colorized according to the extraction region, with blue arrows denoting the  $2\sigma$  upper limit adopted for regions where the average surface brightness is below  $3\sigma$ . The dashed blue indicates the  $1\sigma$  level. The dashed green line shows the best-fitting power-law relation (equation 3) derived using LINMIX, with the  $1\sigma$  uncertainty region shown in the shaded green. The slope of the best-fitting power law is  $b_{1283 \text{ MHz}} = 1.63^{+0.10}_{-0.10}$  at 1283 MHz and  $b_{145 \text{ MHz}} = 1.20^{+0.13}_{-0.11}$  at 145 MHz.

**Table 3.** Summary of results for our Linmix fitting routines, fitting the point-to-point correlation between X-ray surface brightness and either the radio surface brightness at the listed frequency or spectral index, as indicated in the first column.  $b$  is the best-fitting correlation slope for the plane, and  $r_S$  and  $r_P$  are, respectively, the Spearman and Pearson correlation coefficient for each plane.

Image	Slope $b$	Spearman coeff. $r_S$	Pearson coeff. $r_P$
1283 MHz	$1.63^{+0.10}_{-0.10}$	0.90	0.94
145 MHz	$1.20^{+0.13}_{-0.11}$	0.84	0.86
$\alpha$	$0.59^{+0.11}_{-0.11}$	0.67	0.62

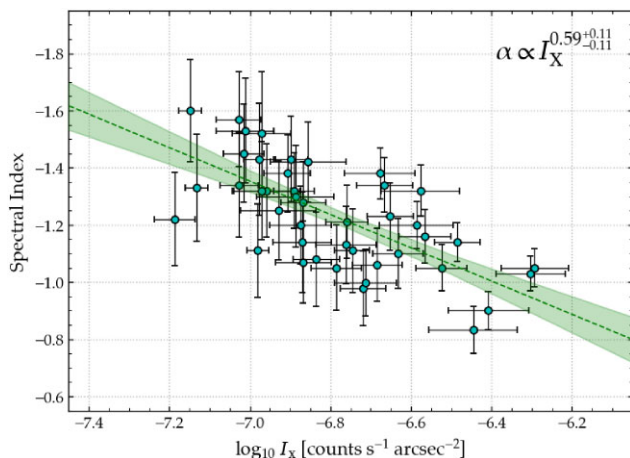


**Figure 11.** Radio spectral index/X-ray surface brightness correlation ( $\alpha_{145 \text{ MHz}}/I_X$ ) for the Abell 1413 mini-halo at 15 arcsec resolution. Note the inverted y-axis to facilitate comparison with previous similar studies. The dashed green line shows the best fit to equation (4), derived using LINMIX, and the shaded green region shows the  $1\sigma$  uncertainty. The slope is  $b = 0.59^{+0.11}_{-0.11}$ .

no change in the  $I_R/I_X$  correlation slope with frequency (respectively Ignesi et al. 2020; Biava et al. 2021; Riseley et al. 2022a).

Interpretation of the  $I_R/I_X$  and  $\alpha/I_X$  correlations requires careful consideration. However, broadly speaking the steepening of the  $I_R/I_X$  correlation toward higher frequencies as well as the slope of the  $\alpha/I_X$  correlation both imply a steepening spectral index with increasing radius. Such a steepening would arise naturally in an acceleration scenario where turbulence plays a significant role in powering the diffuse emission, as has been seen in some radio haloes (e.g. Rajpurohit et al. 2021a). However, this is the first clear confirmation of a radially steepening mini-halo spectrum.

## 5 ON THE NATURE OF THE MECHANISM POWERING THE MINI-HALO IN ABELL 1413

Our census has the overarching aim of investigating and understanding the underlying mechanism responsible for generating mini-haloes. We aim to answer the question of whether the secondary electron model (hadronic collisions between relativistic protons and thermal protons generating CRE) or the primary electron model (acceleration of electrons to relativistic energies by cluster-scale turbulence) is responsible, or whether some form of hybrid scenario predicts properties that are more consistent with our observations.

Similar to our previous study of MS 1455.0+2232, the evidence accumulated from our study of Abell 1413 is mixed. The superlinear  $I_R/I_X$  correlation arises naturally within the secondary electron model, although the primary model can also replicate a superlinear slope depending on the nature of the turbulence.

The numerous active radio galaxies associated with Abell 1413, which are distributed across much of the cluster volume, would naturally provide a source of relativistic protons responsible for generation of CRE via the secondary electron model.

On the other hand, the asymmetry of the mini-halo, which is elongated in the North/South direction, and evidence of large-scale disruption in the ICM – the disturbed BCG, substructure in the galaxy distribution, elongated X-ray surface brightness distribution,

and ‘warm core’ – all suggest that turbulence is likely present on large scales in the ICM. Similarly, the non-uniformity of the spectral index and the tentative evidence of multiple components in the mini-halo would arise more naturally under the primary model, as turbulence is inherently an intermittent process in both spatial and temporal terms.

Overall, we cannot form strong conclusions on the mechanism responsible for the generation of the mini-halo in Abell 1413. Both mechanisms are able to replicate some of the observed properties, but neither mechanism reproduces all of them comprehensively. While on balance the evidence somewhat favours an interpretation of the turbulent acceleration framework, it is likely that both mechanisms are active to some extent.

### 5.1 A simple mathematical framework for hybrid models

Hybrid models have been previously proposed by several authors in the past, predominantly in the context of radio haloes (e.g. Brunetti & Blasi 2005; Brunetti & Lazarian 2011; Cassano et al. 2012; Zandanel et al. 2014; Pinzke, Oh & Pfrommer 2017). Specifically, the models presented by Brunetti & Blasi (2005) and Brunetti & Lazarian (2011) discuss the models most relevant in the context of our census: CRp and their secondary electrons undergoing re-acceleration by turbulence. In light of our observational results it is prudent to further the investigation of hybrid models and present a simple mathematical framework for the expected point-to-point correlation slope in this scenario.

To determine the correlation slope predicted by a hybrid scenario, we need to determine the predicted relation between the X-ray emissivity  $\epsilon_X$  and the radio emissivity  $\epsilon_R$ . These two quantities take the following form:

$$\epsilon_X \propto n_{\text{ICM}}^2 \quad (5a)$$

$$\epsilon_R \propto F_t \eta_e \frac{B^2}{B^2 + B_{\text{IC}}^2}, \quad (5b)$$

where  $n_{\text{ICM}}$  is the number density of thermal particles in the ICM,  $B$  is the magnetic field strength, and  $B_{\text{IC}}$  is the inverse-Compton magnetic field strength (e.g. Brunetti & Vazza 2020).  $F_t$  is the turbulent flux defined as:

$$F_t \propto n_{\text{ICM}} \frac{\delta V_t^3}{L_t},$$

where  $L_t$  is the turbulence length scale and  $\delta V_t^3$  is the dispersion of the turbulent velocity field on that scale. During cluster mergers and interactions, it is generally expected that the turbulence occurs on scales of the cluster core, i.e.  $L_t \simeq 0.1$  to  $0.4$  Mpc (e.g. Vazza et al. 2009). The acceleration efficiency  $\eta_e$  is defined as:

$$\eta_e \propto F_t^{-1} \int d^3p \frac{E}{p^2} \frac{\partial}{\partial p} \left( p^2 D_{pp} \frac{\partial f}{\partial p} \right) \simeq \frac{U_{\text{CRE}} D_{pp}}{F_t p^2},$$

where  $U_{\text{CRE}}$  is the energy density of CRE,  $p$  is the particle momentum, and  $D_{pp}$  is the momentum diffusion coefficient (e.g. Brunetti & Lazarian 2007; Brunetti & Jones 2014, and references therein). Substituting these definitions into equation (5b) we derive:

$$\epsilon_R \propto U_{\text{CRE}} \frac{D_{pp}}{p^2} \frac{B^2}{B^2 + B_{\text{IC}}^2}. \quad (6)$$

Taking a magnetic field strength that follows the relation  $B^2 \propto n_{\text{ICM}}$  and using equation (5a) we find that:

$$\epsilon_R \propto U_{\text{CRE}} \frac{D_{pp}}{p^2} \frac{1}{1 + \left( \frac{B_{\text{IC}}^2}{B_0^2} \right) (\epsilon_X)^{-1/2}}, \quad (7)$$

where  $B_0$  is the central magnetic field strength. In the case where we have a hybrid model, we have a CRE energy density  $U_{\text{CRE}}$  that is a function of both the ICM number density  $n_{\text{ICM}}$  and the number density of cosmic ray protons  $n_{\text{CRp}}$ :

$$U_{\text{CRE}} \propto n_{\text{ICM}} n_{\text{CRp}} \quad (8)$$

and hence equation (7) becomes:

$$\epsilon_R \propto \left( n_{\text{CRp}} \frac{D_{pp}}{p^2} \right) \frac{\epsilon_X^{1/2}}{1 + \left( \frac{B_{\text{IC}}^2}{B_0^2} \right) (\epsilon_X)^{-1/2}}. \quad (9)$$

If we assume the CRp population in the ICM is dominated by injection from the AGN of the central radio BCG, and assume for simplicity a spatial diffusion coefficient  $\kappa_0$  which is both energy-independent and constant with respect to distance from the injection source, the CRp number density in the ICM  $n_{\text{CRp}}$  is given by:

$$n_{\text{CRp}} \propto \frac{Q_{\text{CRp}}}{\kappa_0 r},$$

where  $r$  is the radius and  $Q_{\text{CRp}}$  is the injection rate from the radio BCG. Substituting this definition into equation (9) and normalizing by the central values of  $\epsilon_R$  and  $\epsilon_X$ , respectively  $\epsilon_{R,0}$  and  $\epsilon_{X,0}$  we find that:

$$\frac{\epsilon_R}{\epsilon_{R,0}} \propto \frac{1}{r} \left( \frac{Q_{\text{CRp}} D_{pp}}{\kappa_0 p^2} \right) \left( \frac{(\epsilon_X/\epsilon_{X,0})^{1/2}}{1 + \left( \frac{B_{\text{IC}}^2}{B_0^2} \right) (\epsilon_X/\epsilon_{X,0})^{-1/2}} \right), \quad (10)$$

where the quantity inside the first set of brackets is constant, and in the case where  $B_0^2 \gg B_{\text{IC}}^2$ , we find that:

$$\frac{\epsilon_R}{\epsilon_{R,0}} \propto \frac{1}{r} \left( \frac{\epsilon_X}{\epsilon_{X,0}} \right) \quad (11)$$

and hence equation (11) indicates that the hybrid scenario predicts a superlinear correlation between the radio and X-ray emissivities, and therefore in the  $I_R/I_X$  plane. This simple mathematical framework suggests that the superlinear point-to-point correlation slope reported here for Abell 1413 and previously for MS 1455.0+2232 (Riseley et al. 2022a) are both compatible with a hybrid scenario.

## 6 CONCLUSIONS

This paper is the second in a series of papers presenting the results from a ‘MeerKAT-meets-LOFAR’ mini-halo census, covering 13 clusters hosting known mini-haloes that are visible to both MeerKAT and LOFAR for long-track observations (typically 5.5 h on-source per observing run).

We have presented new MeerKAT L-band (1283 MHz) and LOFAR HBA (145 MHz) observations of the galaxy cluster Abell 1413, which hosts a known mini-halo. We have combined our radio data with archival *Chandra* observations, enabling us to perform a detailed comparison of the thermal and non-thermal properties of this intriguing cluster.

Our new, deep radio observations allow us to achieve more sensitive results than previous studies of this cluster. At full resolution we detect many compact radio sources in the vicinity of Abell 1413 as well as several tailed radio galaxies that are either likely or confirmed cluster-members. After subtracting the contaminating sources and tapering our data to enhance our sensitivity to diffuse radio emission, we detect faint and highly extended radio emission from the ‘mini’-halo up to  $\sim 584$  kpc (and at least 449 kpc) at 1283 MHz.

Measuring from our source-subtracted maps at 15 arcsec resolution and integrating over the region where we are most confident in our source subtraction, we derive a total integrated flux density



of  $S_{1283\text{ MHz}} = 3.23 \pm 0.17$  mJy and  $S_{145\text{ MHz}} = 29.5 \pm 3.4$  mJy. Using these values, we measure an integrated spectral index of  $\alpha_{145\text{ MHz}}^{1283\text{ MHz}} = -1.01 \pm 0.06$ , and derive a  $k$ -corrected 1.4 GHz radio power of  $P_{1.4\text{ GHz}} = (1.50 \pm 0.08) \times 10^{23}$  W Hz $^{-1}$ .

Using our exquisite radio data, we have examined the spatially resolved spectral index profile of the mini-halo. We find an overall global median of  $\langle\alpha\rangle = -1.18 \pm 0.11$ . However, we also find tentative evidence of two different trends: the inner region of the mini-halo appears to show a slightly flatter spectrum with a median value  $\langle\alpha_{\text{in}}\rangle = -0.97 \pm 0.07$ , whereas the outer regions of the mini-halo show a steeper value of  $\langle\alpha_{\text{out}}\rangle = -1.12 \pm 0.13$ . This implies spectral steepening. We emphasize however that this is inconsistent only at the  $\sim 1\sigma$  level, and deeper low-frequency observations would be required to study this further and clarify the underlying emission mechanism.

We have studied the point-to-point correlations between X-ray surface brightness and (i) radio surface brightness at both 1283 and 145 MHz (the  $I_{\text{R}}/I_{\text{X}}$  correlation) and (ii) radio spectral index (the  $\alpha/I_{\text{X}}$  correlation). Our investigation shows that the radio/X-ray surface brightness is strongly correlated, with coefficients in the range  $r = 0.84$  to  $r = 0.94$  depending on frequency and type of coefficient. We find no evidence of departure from a single correlation.

At both frequencies considered here, the slope of the  $I_{\text{R}}/I_{\text{X}}$  correlation is positive, with a value of  $b = 1.63_{-0.10}^{+0.10}$  at 1283 MHz and  $b = 1.20_{-0.11}^{+0.13}$  at 145 MHz. This change in slope with observing frequency may indicate a difference in the non-thermal/thermal connection, although the exact cause of this is as-yet unknown; it may reflect changes in the acceleration mechanism, ambient medium, and/or projection effects. In exploring the  $\alpha/I_{\text{X}}$  correlation, we find a clear correlation with a moderate strength (coefficients 0.62 and 0.67). The slope of this correlation is positive, with a value of  $b_{\alpha} = 0.59_{-0.11}^{+0.11}$ .

While the superlinear slope is a typical signature of the hadronic scenario, our observations also support the interpretation that there is large-scale turbulence at work in Abell 1413. Hence, we investigated a simple mathematical framework which demonstrates that hybrid models – whereby secondary electrons are re-accelerated by turbulence – naturally reproduce a superlinear correlation slope in the  $I_{\text{R}}/I_{\text{X}}$  plane.

## ACKNOWLEDGEMENTS

CJR, NB, and A. Bonafede acknowledge financial support from the ERC Starting Grant ‘DRANOEL’, number 714245. EB acknowledges support from DFG FOR5195. KR acknowledges funding from *Chandra* grant GO0-21112X and ERC starting grant ‘MAGCOW’ number 714196. FL acknowledges financial support from the Italian Minister for Research and Education (MIUR), project FARE, project code R16PR59747, project name FORNAX-B. FL acknowledges financial support from the Italian Ministry of University and Research – Project Proposal CIR01.00010. RT and RJvW acknowledge support from the ERC Starting Grant ‘ClusterWeb’, number 804208. EO and RJvW acknowledge support from the VIDI research programme with project number 639.042.729, which is financed by the Netherlands Organisation for Scientific Research (NWO). We thank our anonymous referee for their feedback on our manuscript, their constructive comments, and their raising of interesting discussion points, which improved the quality of our publication.

The MeerKAT telescope is operated by the South African Radio Astronomy Observatory, which is a facility of the National Research Foundation, an agency of the Department of Science and Innovation. We wish to acknowledge the assistance of the MeerKAT science

operations team in both preparing for and executing the observations that have made our census possible.

LOFAR is the Low Frequency Array designed and constructed by ASTRON. It has observing, data processing, and data storage facilities in several countries, which are owned by various parties (each with their own funding sources), and which are collectively operated by the ILT foundation under a joint scientific policy. The ILT resources have benefited from the following recent major funding sources: CNRS-INSU, Observatoire de Paris and Université d’Orléans, France; BMBF, MIWF-NRW, MPG, Germany; Science Foundation Ireland (SFI), Department of Business, Enterprise and Innovation (DBEI), Ireland; NWO, The Netherlands; The Science and Technology Facilities Council, UK; Ministry of Science and Higher Education, Poland; The Istituto Nazionale di Astrofisica (INAF), Italy.

This research made use of the Dutch national e-infrastructure with support of the SURF Cooperative (e-infra 180169) and the LOFAR e-infra group. This work is co-funded by the EGI-ACE project (Horizon 2020) under Grant number 101017567. The Jülich LOFAR Long Term Archive and the German LOFAR network are both coordinated and operated by the Jülich Supercomputing Centre (JSC), and computing resources on the supercomputer JUWELS at JSC were provided by the Gauss Centre for Supercomputing e.V. (grant CHTB00) through the John von Neumann Institute for Computing (NIC).

This research made use of the University of Hertfordshire high-performance computing facility and the LOFAR-UK computing facility located at the University of Hertfordshire and supported by STFC [ST/P000096/1], and of the Italian LOFAR IT computing infrastructure supported and operated by INAF, and by the Physics Department of Turin university (under an agreement with Consorzio Interuniversitario per la Fisica Spaziale) at the C3S Supercomputing Centre, Italy.

Funding for the Sloan Digital Sky Survey IV has been provided by the Alfred P. Sloan Foundation, the U.S. Department of Energy Office of Science, and the Participating Institutions. SDSS-IV acknowledges support and resources from the Center for High Performance Computing at the University of Utah. The SDSS website is [www.sdss.org](http://www.sdss.org).

SDSS-IV is managed by the Astrophysical Research Consortium for the Participating Institutions of the SDSS Collaboration including the Brazilian Participation Group, the Carnegie Institution for Science, Carnegie Mellon University, Center for Astrophysics|Harvard & Smithsonian, the Chilean Participation Group, the French Participation Group, Instituto de Astrofísica de Canarias, The Johns Hopkins University, Kavli Institute for the Physics and Mathematics of the Universe (IPMU)/University of Tokyo, the Korean Participation Group, Lawrence Berkeley National Laboratory, Leibniz Institut für Astrophysik Potsdam (AIP), Max-Planck-Institut für Astronomie (MPIA Heidelberg), Max-Planck-Institut für Astrophysik (MPA Garching), Max-Planck-Institut für Extraterrestrische Physik (MPE), National Astronomical Observatories of China, New Mexico State University, New York University, University of Notre Dame, Observatório Nacional/MCTI, The Ohio State University, Pennsylvania State University, Shanghai Astronomical Observatory, United Kingdom Participation Group, Universidad Nacional Autónoma de México, University of Arizona, University of Colorado Boulder, University of Oxford, University of Portsmouth, University of Utah, University of Virginia, University of Washington, University of Wisconsin, Vanderbilt University, and Yale University.

Finally, we acknowledge the developers of the following python packages (not mentioned explicitly in the text), which were used

extensively during this project: APLPY (Robitaille & Bressert 2012), ASTROPY (Astropy Collaboration 2013), CMASHER (van der Velden 2020), COLORCET (Kovesi 2015), MATPLOTLIB (Hunter 2007), NUMPY (van der Walt, Colbert & Varoquaux 2011) and SCIPY (Jones et al. 2001).

## DATA AVAILABILITY

The images underlying this article will be shared on reasonable request to the corresponding author. Raw MeerKAT visibilities for both projects SCI-20210212-CR-01 and ‘Mining Minihaloes with MeerKAT’ are in the public domain. All MeerKAT data are accessed via the SARAO archive (<https://apps.sarao.ac.za/katpaws/archive-search>). Raw LOFAR visibilities can be accessed via the LOFAR Long-Term Archive (LTA; <https://lta.lofar.eu>). *Chandra* data are available via the Chandra Data Archive (<https://cxc.harvard.edu/cda/>).

## REFERENCES

- Abazajian K. N. et al., 2009, *ApJS*, 182, 543  
 Ahumada R. et al., 2020, *ApJS*, 249, 3  
 AMI Consortium, 2012, *MNRAS*, 425, 162  
 Ascasibar Y., Markevitch M., 2006, *ApJ*, 650, 102  
 Astropy Collaboration, 2013, *A&A*, 558, A33  
 Baars J. W. M., Genzel R., Pauliny-Toth I. I. K., Witzel A., 1977, *A&A*, 61, 99  
 Baldi A., Ettori S., Mazzotta P., Tozzi P., Borgani S., 2007, *ApJ*, 666, 835  
 Bartalucci I. et al., 2017, *A&A*, 608, A88  
 Biava N. et al., 2021, *MNRAS*, 508, 3995  
 Bonafede A. et al., 2022, *ApJ*, 933, 218  
 Bonamente M., Joy M. K., LaRoque S. J., Carlstrom J. E., Reese E. D., Dawson K. S., 2006, *ApJ*, 647, 25  
 Bonnassieux E., Tasse C., Smirnov O., Zarka P., 2018, *A&A*, 615, A66  
 Botteon A., Gastaldello F., Brunetti G., 2018a, *MNRAS*, 476, 5591  
 Botteon A. et al., 2018b, *MNRAS*, 478, 885  
 Botteon A. et al., 2019, *A&A*, 622, A19  
 Botteon A. et al., 2020, *ApJ*, 897, 93  
 Botteon A. et al., 2022, *A&A*, 660, A78  
 Botteon A., Markevitch M., van Weeren R. J., Brunetti G., Shimwell T. W., 2023, *A&A*, 674, A53  
 Bravi L., Gitti M., Brunetti G., 2016, *MNRAS*, 455, L41  
 Briggs D. S., 1995, PhD Thesis. The New Mexico Institute of Mining and Technology, Socorro, NM  
 Brown S., Rudnick L., 2011, *MNRAS*, 412, 2  
 Brunetti G., Blasi P., 2005, *MNRAS*, 363, 1173  
 Brunetti G., Jones T. W., 2014, *Int. J. Mod. Phys. D*, 23, 1430007  
 Brunetti G., Lazarian A., 2007, *MNRAS*, 378, 245  
 Brunetti G., Lazarian A., 2011, *MNRAS*, 410, 127  
 Brunetti G., Vazza F., 2020, *Phys. Rev. Lett.*, 124, 051101  
 Brunetti G., Blasi P., Cassano R., Gabici S., 2004, *MNRAS*, 350, 1174  
 Bruno L. et al., 2021, *A&A*, 650, A44  
 Camilo F. et al., 2018, *ApJ*, 856, 180  
 Campitiello M. G. et al., 2022, *A&A*, 665, A117  
 Cassano R., Brunetti G., Norris R. P., Röttgering H. J. A., Johnston-Hollitt M., Trasatti M., 2012, *A&A*, 548, A100  
 Castagné D., Soucaïl G., Pointecouteau E., Cappi A., Maurogordato S., Benoist C., Ferrari C., 2012, *A&A*, 548, A18  
 Duchesne S. W., Johnston-Hollitt M., Zhu Z., Wayth R. B., Line J. L. B., 2020, *Publ. Astron. Soc. Austr.*, 37, e037  
 Duchesne S. W., Johnston-Hollitt M., Bartalucci I., Hodgson T., Pratt G. W., 2021a, *Publ. Astron. Soc. Austr.*, 38, e005  
 Duchesne S. W., Johnston-Hollitt M., Wilber A. G., 2021b, *Publ. Astron. Soc. Austr.*, 38, e031  
 Duchesne S. W., Johnston-Hollitt M., Bartalucci I., 2021c, *Publ. Astron. Soc. Austr.*, 38, e053  
 Duchesne S. W., Johnston-Hollitt M., Riseley C. J., Bartalucci I., Keel S. R., 2022, *MNRAS*, 511, 3525  
 Ettori S., Gastaldello F., Leccardi A., Molendi S., Rossetti M., Buote D., Meneghetti M., 2010, *A&A*, 524, A68  
 Ghizzardi S., De Grandi S., Molendi S., 2014, *A&A*, 570, A117  
 Ghizzardi S., Rossetti M., Molendi S., 2010, *A&A*, 516, A32  
 Giacintucci S., Markevitch M., Venturi T., Clarke T. E., Cassano R., Mazzotta P., 2014, *ApJ*, 781, 9  
 Giacintucci S., Markevitch M., Cassano R., Venturi T., Clarke T. E., Brunetti G., 2017, *ApJ*, 841, 71  
 Giacintucci S., Markevitch M., Cassano R., Venturi T., Clarke T. E., Kale R., Cuciti V., 2019, *ApJ*, 880, 70  
 Gitti M., Brunetti G., Setti G., 2002, *A&A*, 386, 456  
 Govoni F., Enßlin T. A., Feretti L., Giovannini G., 2001, *A&A*, 369, 441  
 Govoni F., Murgia M., Markevitch M., Feretti L., Giovannini G., Taylor G. B., Carretti E., 2009, *A&A*, 499, 371  
 Grainge K., Jones M., Pooley G., Saunders R., Baker J., Haynes T., Edge A., 1996, *MNRAS*, 278, L17  
 Grainge K., Jones M. E., Pooley G., Saunders R., Edge A., Grainger W. F., Kneissl R., 2002, *MNRAS*, 333, 318  
 Gupta Y. et al., 2017, *Curr. Sci.*, 113, 707  
 Hardcastle M. J. et al., 2016, *MNRAS*, 462, 1910  
 Hoang D. N. et al., 2019, *A&A*, 622, A20  
 Hoang D. N. et al., 2021, *A&A*, 656, A154  
 Hoang D. N. et al., 2022, *A&A*, 665, A60  
 Hoeft M. et al., 2021, *A&A*, 654, A68  
 Hogan M. T. et al., 2015, *MNRAS*, 453, 1201  
 Hoshino A. et al., 2010, *PASJ*, 62, 371  
 Hugo B. V., Perkins S., Merry B., Mauch T., Smirnov O. M., 2022, in Ruiz J. E., Pierfederici F., Teuben P., eds, *ASP Conf. Ser. Vol. 532, Astronomical Data Analysis Software and Systems XXX*. Astron. Soc. Pac., San Francisco, p. 541  
 Humason M. L., Mayall N. U., Sandage A. R., 1956, *AJ*, 61, 97  
 Hunter J. D., 2007, *Comput. Sci. Eng.*, 9, 90  
 Ignesti A., Brunetti G., Gitti M., Giacintucci S., 2020, *A&A*, 640, A37  
 Ignesti A. et al., 2022, *A&A*, 659, A20  
 Intema H. T., van der Tol S., Cotton W. D., Cohen A. S., van Bemmell I. M., Röttgering H. J. A., 2009, *A&A*, 501, 1185  
 Intema H. T., Jagannathan P., Mooley K. P., Frail D. A., 2017, *A&A*, 598, A78  
 Johnson R. E., Zuhone J., Jones C., Forman W. R., Markevitch M., 2012, *ApJ*, 751, 95  
 Jonas J., MeerKAT Team, 2016, in *Proc. Sci., MeerKAT Science: On the Pathway to the SKA*. SISSA, Trieste, Pos#001  
 Jones E., Oliphant T., Peterson P. et al., 2001, *SciPy: Open source scientific tools for Python*. Available at: <http://www.scipy.org/>  
 Józsa G. I. G. et al., 2020, *Astrophysics Source Code Library*, record ascl:2006.014  
 Józsa G. I. G. et al., 2021, *MNRAS*, 501, 2704  
 Kellermann K. I., 1966, *Aust. J. Phys.*, 19, 195  
 Kelly B. C., 2007, *ApJ*, 665, 1489  
 Kempner J. C., Blanton E. L., Clarke T. E., Enßlin T. A., Johnston-Hollitt M., Rudnick L., 2004, in Reiprich T., Kempner J., Soker N., eds, *The Riddle of Cooling Flows in Galaxies and Clusters of Galaxies*. p. 335, available at: <http://www.astro.virginia.edu/coolflow/>  
 Knowles K. et al., 2022, *A&A*, 657, A56  
 Kovesi P., 2015, preprint (arXiv:1509.03700)  
 Lacy M. et al., 2020, *PASP*, 132, 035001  
 LaRoque S. J., Bonamente M., Carlstrom J. E., Joy M. K., Nagai D., Reese E. D., Dawson K. S., 2006, *ApJ*, 652, 917  
 Locatelli N. T. et al., 2020, *MNRAS*, 496, L48  
 Lusetti G., 2021, *Tesi di laurea, Alma Mater Studiorum – Università di Bologna, Bologna*. Available at: <http://amslaurea.unibo.it/23747/>  
 Lusetti G. et al., 2023, preprint (arXiv:2308.01884)  
 Machado R. E. G., Lima Neto G. B., 2015, *MNRAS*, 447, 2915  
 Makhathini S., 2018, PhD thesis, Rhodes University, South Africa  
 Markevitch M., Vikhlinin A., 2007, *Phys. Rep.*, 443, 1

- Mauch T. et al., 2020, *ApJ*, 888, 61
- Mazzotta P., Giacintucci S., 2008, *ApJ*, 675, L9
- Mazzotta P., Markevitch M., Forman W. R., Jones C., Vikhlinin A., VanSpeybroeck L., 2001a, preprint (arXiv:astro-ph/0108476)
- Mazzotta P., Markevitch M., Vikhlinin A., Forman W. R., David L. P., van Speybroeck L., 2001b, *ApJ*, 555, 205
- Mohan N., Rafferty D., 2015, Astrophysics Source Code Library, record ascl:1502.007
- Morrison G. E., Owen F. N., Ledlow M. J., Keel W. C., Hill J. M., Voges W., Herter T., 2003, *ApJS*, 146, 267
- Noonan T. W., 1972, *AJ*, 77, 9
- Norris R. P. et al., 2011, *Publ. Astron. Soc. Austr.*, 28, 215
- Norris R. P. et al., 2021, *Publ. Astron. Soc. Austr.*, 38, e046
- Offringa A. R., Smirnov O., 2017, *MNRAS*, 471, 301
- Offringa A. R. et al., 2014, *MNRAS*, 444, 606
- Osinga E. et al., 2022, *A&A*, 665, A71
- Owers M. S., Nulsen P. E. J., Couch W. J., Markevitch M., 2009, *ApJ*, 704, 1349
- Paterno-Mahler R., Blanton E. L., Randall S. W., Clarke T. E., 2013, *ApJ*, 773, 114
- Pfrommer C., Enßlin T. A., 2004, *A&A*, 413, 17
- Pinzke A., Oh S. P., Pfrommer C., 2017, *MNRAS*, 465, 4800
- Planck Collaboration XVI, 2014, *A&A*, 571, A29
- Pointecouteau E., Arnaud M., Pratt G. W., 2005, *A&A*, 435, 1
- Pratt G. W., Arnaud M., 2002, *A&A*, 394, 375
- Raja R. et al., 2020, *MNRAS*, 493, L28
- Rajpurohit K. et al., 2018, *ApJ*, 852, 65
- Rajpurohit K. et al., 2021a, *A&A*, 646, A135
- Rajpurohit K. et al., 2021b, *A&A*, 654, A41
- Reddy S. H. et al., 2017, *J. Astron. Instrum.*, 6, 1641011
- Richard-Laferrrière A. et al., 2020, *MNRAS*, 499, 2934
- Riseley C. J. et al., 2022a, *MNRAS*, 512, 4210
- Riseley C. J. et al., 2022b, *MNRAS*, 515, 1871
- Robitaille T., Bressert E., 2012, Astrophysics Source Code Library, record ascl:1208.017
- Rossetti M., Molendi S., 2010, *A&A*, 510, A83
- Rossetti M., Eckert D., De Grandi S., Gastaldello F., Ghizzardi S., Roediger E., Molendi S., 2013, *A&A*, 556, A44
- Rossetti M., Gastaldello F., Eckert D., Della Torre M., Pantiri G., Cazzoletti P., Molendi S., 2017, *MNRAS*, 468, 1917
- Sanders J. S., Fabian A. C., Smith R. K., 2011, *MNRAS*, 410, 1797
- Sanders J. S., Fabian A. C., Russell H. R., Walker S. A., Blundell K. M., 2016, *MNRAS*, 460, 1898
- Sanders J. S. et al., 2022, *A&A*, 661, A36
- Savini F. et al., 2018, *MNRAS*, 478, 2234
- Savini F. et al., 2019, *A&A*, 622, A24
- Scaife A. M. M., Heald G. H., 2012, *MNRAS*, 423, L30
- Seth R., O'Sullivan E., Sebastian B., Raychaudhury S., Schellenberger G., Haines C. P., 2022, *MNRAS*, 513, 3273
- Shimwell T. W. et al., 2017, *A&A*, 598, A104
- Shimwell T. W. et al., 2019, *A&A*, 622, A1
- Shimwell T. W. et al., 2022, *A&A*, 659, A1
- Smirnov O. M., Tasse C., 2015, *MNRAS*, 449, 2668
- Snowden S. L., Mushotzky R. F., Kuntz K. D., Davis D. S., 2008, *A&A*, 478, 615
- Tasse C., 2014, *A&A*, 566, A127
- Tasse C. et al., 2018, *A&A*, 611, A87
- Tasse C. et al., 2021, *A&A*, 648, A1
- Timmerman R., van Weeren R. J., McDonald M., Ignesti A., McNamara B. R., Hlavacek-Larrondo J., Röttgering H. J. A., 2021, *A&A*, 646, A38
- Tingay S. J. et al., 2013, *Publ. Astron. Soc. Austr.*, 30, e007
- Trehaeven K. S. et al., 2023, *MNRAS*, 520, 4410
- Vacca V., Govoni F., Murgia M., Giovannini G., Feretti L., Tugnoli M., Verheijen M. A., Taylor G. B., 2011, *A&A*, 535, A82
- Vacca V. et al., 2022, *MNRAS*, 511, 3389
- van der Velden E., 2020, *J. Open Source Softw.*, 5, 2004
- van der Walt S., Colbert S. C., Varoquaux G., 2011, *Comput. Sci. Eng.*, 13, 22
- van Diepen G., Dijkema T. J., Offringa A., 2018, Astrophysics Source Code Library, record ascl:1804.003
- van Haarlem M. P. et al., 2013, *A&A*, 556, A2
- van Weeren R. J., de Gasperin F., Akamatsu H., Brügger M., Feretti L., Kang H., Stroe A., Zandanel F., 2019, *Space Sci. Rev.*, 215, 16
- van Weeren R. J. et al., 2021, *A&A*, 651, A115
- Vazza F., Brunetti G., Kritsuk A., Wagner R., Gheller C., Norman M., 2009, *A&A*, 504, 33
- Venturi T. et al., 2017, *A&A*, 603, A125
- Venturi T. et al., 2022, *A&A*, 660, A81
- Vikhlinin A., Markevitch M., Murray S. S., Jones C., Forman W., Van Speybroeck L., 2005, *ApJ*, 628, 655
- Whelan B. et al., 2022, *A&A*, 663, A171
- Wilber A. et al., 2018, *MNRAS*, 473, 3536
- Wilber A. G., Johnston-Hollitt M., Duchesne S. W., Tasse C., Akamatsu H., Intema H., Hodgson T., 2020, *Publ. Astron. Soc. Austr.*, 37, e040
- Xie C. et al., 2020, *A&A*, 636, A3
- Zandanel F., Pfrommer C., Prada F., 2014, *MNRAS*, 438, 124
- ZuHone J. A., Markevitch M., Brunetti G., Giacintucci S., 2013, *ApJ*, 762, 78
- ZuHone J. A., Brunetti G., Giacintucci S., Markevitch M., 2015, *ApJ*, 801, 146

## APPENDIX A: PROPERTIES OF IDENTIFIED SOURCES

**Table A1.** Flux density measurements  $S$  at 1283 and 145 MHz, as well as the corresponding radio spectral index  $\alpha$  for sources identified with yellow ‘+’ signs in Fig. 2 of the main paper. Point sources were modelled using a simple single Gaussian fit; extended source flux densities were derived by integrating above the  $3\sigma_{\text{local}}$  level. We note that for clarity the marker for source 14, the embedded head-tail radio galaxy, is not shown in Fig. 2. This source, along with the BCG can be seen in Fig. 4; the flux density measurements for the BCG are presented in Table 2 and Fig. 5. Cross-identifications with Sloan Digital Sky Survey (SDSS) optical counterparts are listed where available, along with redshift measurements ( $z$ ). We quote spectroscopic redshifts where present, photometric redshifts otherwise (identified with a ‘ $p$ ’). Galaxies where the association and/or the SDSS photometry is uncertain are marked by a ‘ $u$ ’.

ID	Right ascension (J2000)	Declination (J2000)	$S_{1283 \text{ MHz}}$ (mJy)	$S_{145 \text{ MHz}}$ (mJy)	$\alpha$	Cross-ID	$z$	Notes
01	11:55:08.94	+23:26:22.6	$26.63 \pm 1.33$	$178 \pm 18$	$-0.87 \pm 0.05$	SDSS J115508.97+232623.4	0.144	–
02	11:55:12.73	+23:22:53.9	$0.049 \pm 0.006$	–	–	SDSS J115512.73+232254.3	–	–
03	11:55:13.37	+23:24:29.2	$0.090 \pm 0.007$	–	–	–	–	–
04	11:55:13.49	+23:22:47.5	$0.053 \pm 0.005$	–	–	–	–	–
05	11:55:13.87	+23:23:27.1	$0.039 \pm 0.004$	–	–	–	–	–
06	11:55:14.00	+23:26:31.1	$0.110 \pm 0.022$	$1.11 \pm 0.13$	$-1.06 \pm 0.11$	SDSS J115513.96+232630.7	0.171	$p$
07	11:55:14.82	+23:26:37.9	$0.213 \pm 0.017$	$0.98 \pm 0.13$	$-0.70 \pm 0.07$	SDSS J115515.46+232635.1	0.666	$p, u$
08	11:55:15.11	+23:24:01.4	$0.46 \pm 0.02$	$1.10 \pm 0.12$	$-0.40 \pm 0.05$	–	–	–
09	11:55:15.47	+23:25:39.9	$0.19 \pm 0.02$	$0.68 \pm 0.39$	$-0.58 \pm 0.27$	SDSS J115515.47+232539.6	0.176	$p$
10	11:55:15.92	+23:26:25.2	$0.294 \pm 0.021$	$1.37 \pm 0.26$	$-0.71 \pm 0.09$	SDSS J115516.27+232627.2	–	$u$
11	11:55:16.54	+23:21:43.6	$0.063 \pm 0.005$	–	–	SDSS J115516.62+232142.6	–	–
12	11:55:17.06	+23:23:55.1	$0.10 \pm 0.02$	–	–	SDSS J115517.13+232352.6	0.149	$p$
13	11:55:17.12	+23:22:14.7	$1.89 \pm 0.10$	$16.42 \pm 1.75$	$-0.99 \pm 0.05$	SDSS J115518.60+232424.0	0.139	–
14	11:55:18.64	+23:24:21.2	$2.39 \pm 0.12$	$12.16 \pm 1.33$	$-0.75 \pm 0.06$	SDSS J115518.60+232424.0	0.139	–
15	11:55:18.56	+23:22:03.7	$0.058 \pm 0.006$	–	–	SDSS J115521.05+232319.2	0.351	$p, u$
16	11:55:19.26	+23:26:51.3	$0.330 \pm 0.017$	$3.56 \pm 0.45$	$-1.09 \pm 0.06$	SDSS J115519.28+232651.6	0.464	$p$
17	11:55:20.84	+23:23:18.9	$0.051 \pm 0.006$	–	–	–	–	–
18	11:55:21.12	+23:27:24.3	$0.108 \pm 0.007$	$0.86 \pm 0.10$	$-0.95 \pm 0.06$	SDSS J115521.09+232723.6	0.289	$p$
19	11:55:21.42	+23:23:36.1	$0.12 \pm 0.02$	$1.04 \pm 0.13$	$-0.99 \pm 0.10$	SDSS J115521.97+232335.5	0.373	$u$
20	11:55:22.16	+23:26:18.8	$0.086 \pm 0.006$	$0.51 \pm 0.06$	$-0.82 \pm 0.06$	–	–	–
21	11:55:23.04	+23:23:04.4	$0.25 \pm 0.01$	–	–	–	–	–
22	11:55:23.17	+23:24:25.0	$0.049 \pm 0.005$	$0.85 \pm 0.13$	$-1.31 \pm 0.08$	SDSS J115523.03+232425.4	0.140	$u$
23	11:55:23.83	+23:26:59.5	$0.071 \pm 0.013$	–	–	SDSS J115524.30+232654.4	0.706	$p, u$
24	11:55:24.15	+23:24:43.0	$0.21 \pm 0.02$	$0.91 \pm 0.39$	$-0.67 \pm 0.20$	SDSS J115524.16+232443.0	1.775	$p, u$
25	11:55:25.13	+23:26:40.4	$0.080 \pm 0.005$	–	–	SDSS J115525.19+232640.9	0.770	$p$

This paper has been typeset from a  $\text{\TeX}/\text{\LaTeX}$  file prepared by the author.